

Review

# A Mini Review: Recent Advances in Asymmetrically Coordinated Atom Sites for High-Efficiency Hydrogen Evolution Reaction

Junyang Ding <sup>1,2</sup>, Wenxian Liu <sup>3,\*</sup>, Shusheng Zhang <sup>4</sup>, Jun Luo <sup>1,5</sup> and Xijun Liu <sup>2,\*</sup> 

<sup>1</sup> Institute for New Energy Materials and Low-Carbon Technologies, School of Materials Science and Engineering, Tianjin University of Technology, Tianjin 300384, China

<sup>2</sup> State Key Laboratory of Featured Metal Materials and Life-Cycle Safety for Composite Structures, School of Resource, Environments and Materials, Nanning 530004, China

<sup>3</sup> College of Materials Science and Engineering, Zhejiang University of Technology, 18 Chaowang Road, Hangzhou 310014, China

<sup>4</sup> College of Chemistry, Zhengzhou University, Zhengzhou 450001, China

<sup>5</sup> Shensi Laboratory, Shenzhen Institute for Advanced Study, University of Electronic Science and Technology of China, Longhua District, Shenzhen 518110, China

\* Correspondence: liuwx@zjut.edu.cn (W.L.); xjliu@tjut.edu.cn (X.L.)

**Abstract:** Energy is the substance foundation of human society. Single-atom catalysts (SACs) have emerged as promising electrode materials in the energy field owing to their unique characteristics. It was demonstrated that the hydrogen evolution reaction (HER) performance of SACs relies on the metal-centric species and the corresponding local coordination engineering. Herein, the recent progress relating to asymmetric atomic catalysts for the HER is reviewed, including low coordination, heteroatomic coordination, and bimetallic coordination. In addition, the connection between the coordination structures and the presented electrocatalytic performance was discussed. The main challenges that need to be addressed for the asymmetric atomic catalysts in the HER are summarized. Finally, some insights into the development of high-quality asymmetric atomic catalysts are included.

**Keywords:** asymmetric atom sites; coordination environment; hydrogen evolution reaction; catalyst design



**Citation:** Ding, J.; Liu, W.; Zhang, S.; Luo, J.; Liu, X. A Mini Review: Recent Advances in Asymmetrically Coordinated Atom Sites for High-Efficiency Hydrogen Evolution Reaction. *Energies* **2023**, *16*, 2664. <https://doi.org/10.3390/en16062664>

Academic Editor: Eugenio Meloni

Received: 21 February 2023

Revised: 10 March 2023

Accepted: 10 March 2023

Published: 12 March 2023



**Copyright:** © 2023 by the authors. Licensee MDPI, Basel, Switzerland. This article is an open access article distributed under the terms and conditions of the Creative Commons Attribution (CC BY) license (<https://creativecommons.org/licenses/by/4.0/>).

## 1. Introduction

With the objectives of carbon neutrality being established across multiple countries and regions, the utilization of renewable energy sources, such as hydrogen, wind, solar, and tidal energy, is paramount for the sustainment of present day society [1–7]. High-performance catalysts are the key to constructing inexpensive, high-efficiency energy storage and conversion systems since they allow for altering the reaction path, reducing the activation energy barrier, and improving the reaction rate [8–12]. Typically, catalysts are categorized into two groups: homogeneous and heterogeneous [13–17]. Homogeneous catalysts are located within the reactants in one phase and maximizes the effectiveness of the interaction. However, their widespread practical adoption is hampered since it is challenging to isolate them from the other reaction components [18–21]. Heterogeneous catalysts reside in the distinct phases from the reactants during the reaction. They often comprise metal particles of uneven size and are still employed extensively in mass manufacturing due to their low cost and good recoverability. However, they perform poorly regarding their activity, selectivity, and atom consumption [22–26].

Among the various hydrogen evolution reaction (HER) catalysts involved in the electrolysis of the H<sub>2</sub>O molecule, single-atom catalysts (SACs) on diverse carriers (organic-, metal-, and carbon-based materials) have emerged in recent years that are capable of successfully incorporating the respective merits of the homogeneous and heterogeneous

catalysts, such as well-defined electronic structures, defined geometric configurations, virtually 100% atomic availability, desirable catalytic efficiency, and recoverability [27–32]. Moreover, researchers now have gained a deeper insight into the atomic centers' neighboring environment due to the continuous enhancement and advancement of characterization techniques such as the Fourier transform infrared (FTIR) spectra, X-ray photoelectron spectroscopy (XPS), X-ray absorption fine structure (XAFS), and transmission electron microscopy (TEM), etc. [33–35]. Therefore, contrary to the conventional symmetric atomic sites, researchers have attempted to construct diverse SACs, e.g., low coordination, lateral heteroatomic coordination, axial heteroatomic coordination, and dual-metal SACs, to obtain asymmetric atomic sites (Figure 1) [36–38]. The asymmetric coordination configuration can precisely modulate the active moieties' electronic distribution and its adsorption-desorption behavior for the key reaction intermediate of  $H^*$ , which could decrease the original overpotential, enhance the catalytic activity, and accelerate the electrocatalytic hydrogen production [39–41]. This demonstrates that apart from the metal catalytic center, the geometric coordination structures around the center considerably influence the reaction energy barriers and pathways [42–44].

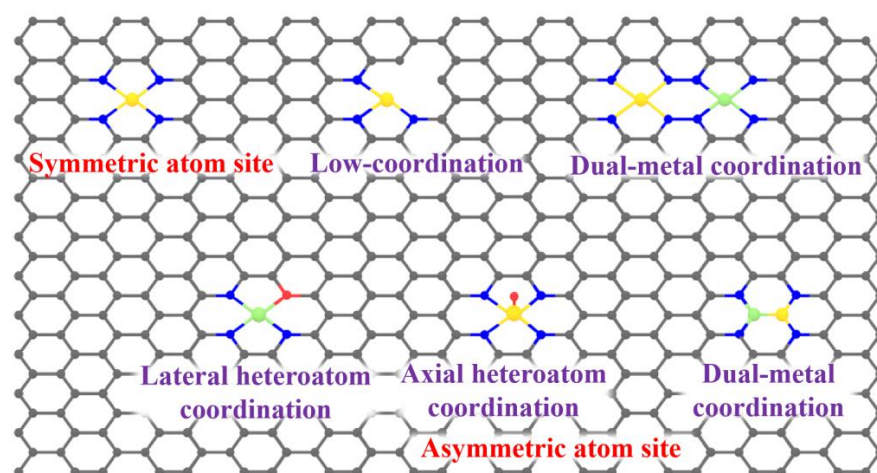
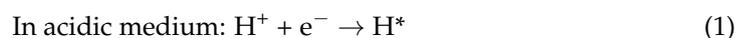


**Figure 1.** Model illustration for the symmetric/asymmetric atom sites (yellow and green, metal atom; blue, N atom; gray, C atom; red, heteroatom, such as O, P, S etc.).

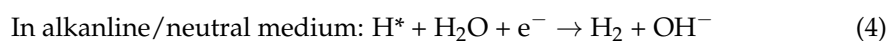
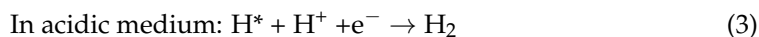
In this mini review, the merits of the asymmetric atom catalysts in the HER have been systematically described. Three types of asymmetrically atomic catalysts with carbon-based supports were presented, namely, low-coordination structures, lateral/axial heteroatomic coordination structures, and dual-metal coordination structures. In addition, the organic/metallic support-loaded asymmetrical sites were briefly introduced. Finally, the difficulties and openings of the asymmetric atomic catalysts toward electrocatalytic hydrogen generation have been further prospected.

## 2. The Mechanistic Principles of HER

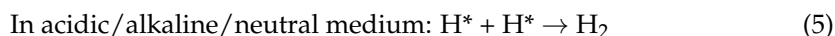
The HER, occurring at the cathode, is a half reaction in water splitting that undergoes a two-electron transfer process. The two reaction mechanisms, i.e., the Volmer–Heyrovsky and Volmer–Tafel, are as follows (\* represents the active site) [45–47]: Volmer step



Heyrovsky step



Tafel step



The initial Volmer reaction can form absorbed  $\text{H}^*$  from  $\text{H}^+$  ions or  $\text{H}_2\text{O}$  molecules in all kinds of electrolytes. The selectivity of the next reaction step, i.e., the Heyrovsky or Tafel steps, depends on the  $\text{H}^*$  coverage of the catalytic sites. Generally, the Heyrovsky step occurs when there is a low  $\text{H}^*$  coverage, otherwise the Tafel step occurs [48–50]. The rate-determining steps can be judged by measuring the Tafel slope values, where 120, 40, and 30  $\text{mV dec}^{-1}$  correspond to Volmer, Heyrovsky, or Tafel reactions, respectively [51–53]. Moreover, the low  $\text{H}^*$  adsorption free energy ( $|\Delta G_{\text{H}^*}|$  close to zero) points toward a better inner activity in the density functional theory [54–57].

### 3. Asymmetric Atom Sites for HER

#### 3.1. Low-Coordination Structure

Generally, the metal centers with low-coordination sites can be grouped into two species, precious metals and non-precious metals, and the corresponding carbon-based carriers are mainly graphene, nitrogen-doped graphene, graphdiyne, and  $\text{C}_3\text{N}_4$ , etc.

For the asymmetric  $\text{MN}_x$ , Zang et al. designed atomic catalysts (Ni-SA/NC) with a Ni- $\text{N}_3$ - $\text{O}_2$  coordination and low overpotentials in both freshwater ( $\eta_{10}$ : 102 mV overpotential at 10  $\text{mA cm}^{-2}$ ) and seawater ( $\eta_{10}$ : 139 mV), demonstrating that low-coordination Ni- $\text{N}_3$  was more beneficial for  $\text{H}_2\text{O}$  dissociation and  $\text{H}^*$  adsorption and was considered as an HER active site (Figure 2a) [58]. Liu et al. discovered that the edge models i.e., Co-2N-armchair, Co-2N-A, Co-2N-zigzag, and Co-2N-Z, were more reactive than the plane model of Co-4N-P for the HER. The edge-rich Co single atoms (E-Co SAs) (Figure 2b) were composed of Co-4N-P (65.49%), Co-2N-A (13.64%), and Co-2N-Z (20.86%), showing a significantly enhanced HER performance account for the edge effect of E-Co SAs ( $\eta_{10}$ : ~59 mV) compared to  $\text{CoN}_4$  SACs ( $\eta_{10}$ : ~111 mV) with an extraordinary durability of 200 h at 500  $\text{mA cm}^{-2}$  (Figure 2c) [59]. For the asymmetric  $\text{MC}_x$ , the defective sites on the carbonaceous supports, similar to the hexa-carbon ring-like hollow sites, were often used as anchor sites for the metal-based single atoms. Meanwhile, Zhang et al. adopted another graphene vacancy for capturing Ni atoms as the SACs, identifying the presence of the common double vacancy aNi@Di-vacancy ( $\text{NiC}_4$ ) and the Stone-Wales graphene defect aNi@5775 ( $\text{NiC}_7$ ), as shown in Figure 2d,e. Differing from the perfect hexagonal ( $\text{NiC}_6$ ) and divacancy Ni site, aNi@5775 demonstrates a higher density in the states close to the benchmarked Fermi level, pointing to stronger interactions between Ni and the key intermediates (e.g.,  $\text{H}^+$  and  $\text{OH}^-$ ) than the divacancy ones, thus noting aNi@D5775 as more favorable for the HER ( $\eta_{10}$ : 70 mV in 0.5 M  $\text{H}_2\text{SO}_4$ ) and OER (Figure 2f,g) [60]. In other works, Ni single atoms were steadily coordinated with neighboring C atoms on nanoporous graphene (np-G), and the atomic resolution HAADF-STEM also clearly suggested this substituted configuration ( $\text{Ni}_{\text{sub}}$ ,  $\text{NiC}_3$ ). Compared the absorbed and defective Ni sites, the substitutional  $\text{Ni}_{\text{sub}}$  exhibited a minimum  $\Delta G_{\text{H}^*}$  and could work as a prominent active center for the HER ( $\eta_{10}$ : ~50 mV in 0.5 M  $\text{H}_2\text{SO}_4$ ) [61]. For an atomic-level identification of the active site properties, Fang et al. examined the structural evolution of Pt in the nitrogen-carbon substrate ( $\text{Pt}_1/\text{N-C}$ ) and revealed a weak interaction between them, with the Pt atom tending to show a low coordination, especially when the coordination number decreased to 2 ( $\text{Pt}_1\text{C}_2-1$   $\text{Pt}_1\text{C}_2-2$ ) when the applied potential was at -0.07 V (Figure 2h). This contributed to a better bonding strength between the Pt atom and the reactant molecule, i.e., a lower coordination number enhanced the activity of the Pt sites ( $\eta_{10}$ : 19 mV in 0.5 M  $\text{H}_2\text{SO}_4$ ; 46 mV in 1.0 M NaOH), as shown in Figure 2i [62]. Wei et al. found that there was a smaller negative  $\Delta G_{\text{H}^*}$  compared to the Pt (111) when the Pt atoms were adsorbed on the defects (Pt<sub>on</sub>SV,  $\text{PtC}_3$ ) or edges (Pt<sub>on</sub>edge,  $\text{PtC}_2$ ) of the graphene of the mesoporous carbon, verifying the enhanced HER activities of the Pt SACs with low-coordination numbers (65 mV at 100  $\text{mA cm}^{-2}$  in 0.5 M  $\text{H}_2\text{SO}_4$ ) [63]. Aside from the graphene and N-doped carbon substrates, the  $\text{C}_3\text{N}_4$  localized  $\text{RuN}_2$  sites with an  $\eta_{10}$  of 140 mV and a graphdiyne anchored four-coordinated

$\text{C}_2\text{-Pt-Cl}_2$  of  $23.64 \text{ A mg}^{-1}$  at  $100 \text{ mV}$  and an overpotential of  $0.5 \text{ M H}_2\text{SO}_4$ , were also reported in the HER electrocatalysis [64,65].

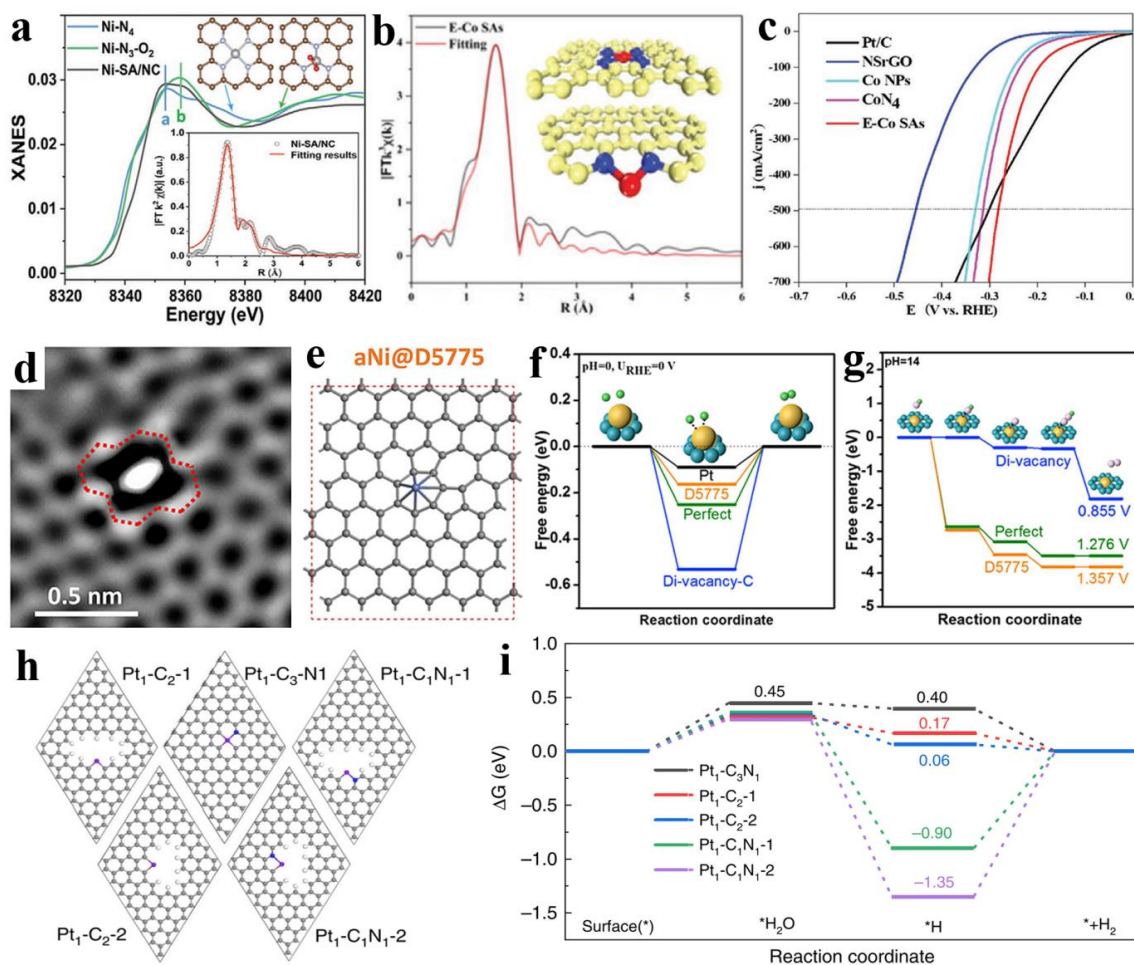


**Figure 2.** (a) X-ray adsorption near-edge structure (XANES) curves of Ni-SAs/NC. Reprinted with permission from ref. [58]. Copyright (2020) Wiley-VCH GmbH. (b) Fourier transform extended X-ray absorption fine structure (FT-EXAFS) fitting curve for E-Co SAs in the R space. (c) Linear sweep voltammetric (LSV) curves in  $1 \text{ M KOH}$ . Reprinted with permission from ref. [59]. Copyright (2021) Wiley-VCH GmbH. (d) High-resolution high-angle annular dark field scanning transmission electron microscopy (HAADF-STEM) images of the defective area with atomic trapped Ni. (e) Coordination structure of a Ni single atom supported on D5775. Energy profiles for the HER (f) and the OER (g). Reprinted with permission from ref. [60]. Copyright (2017) Elsevier Inc. (h) Theory models of the  $\text{Pt}_1\text{-C}_3\text{N}_1$ , two different  $\text{Pt}_1\text{-C}_2$ , and two different  $\text{Pt}_1\text{-C}_1\text{N}_1$  sties. (i) Adsorption free energies toward  $\text{H}_2\text{O}$  and  $\text{H}^*$ . Reprinted with permission from ref. [62]. Copyright (2020) Nature Publishing Group.

Based on the above-mentioned reports, it can be noticed that the low-coordination atom sites were mainly located on the carbon defects/vacancies and edges compared to the perfect-coordination sites. The low-coordinated  $\text{MN}_x\text{C}_y$  was more favorable for  $\text{H}_2\text{O}$  dissociation or  $\text{H}^*$  adsorption, and thus was reasonably considered as the HER active site.

### 3.2. Lateral/Axial Heteroatom Coordination Structure

Heteroatomic coordination is usually composed of two element types (C/N, P/N, B/N, and I/N) or even coexists with multiple elements (C/N/O). Heteroatoms also appear in different coordination shell positions and spatial orientations, increasing the diversity of the modulating metal active centers.

Lu et al. demonstrated that Ru and N co-doped carbon nanowires ( $\eta_{10}$ : 12 mV) outperformed the benchmark 20% platinum/carbon ( $\eta_{10}$ : 49 mV) for the HER in a 1 M KOH alkaline media (Figure 3a). The control experiments and the first-principles principle calculations showed that the HER activity of Ru-NC-700 mainly came from atomically dispersed Ru that coordinated with N and C, while the contribution of the ruthenium NPs was almost negligible. Ru-C<sub>2</sub>N<sub>2</sub> has the finest  $|\Delta G_{H^*}|$  close to zero and was more active than Ru-C<sub>4</sub> and Ru-N<sub>4</sub>, in which the Ru center and the C site served as the catalytic center, while the N site accelerated the hydrogen bonding steps (Figure 3b) [66]. Chen et al. successfully achieved a rational design of the W<sub>1</sub>N<sub>1</sub>C<sub>3</sub> moiety local structure at the atomic level by anchoring the W atom to an N-doped carbon substrate from UiO-66-NH<sub>2</sub> (Figure 3c). The absolute value of  $\Delta G_{H^*}$  on the W<sub>1</sub>N<sub>1</sub>C<sub>3</sub> site was less than other possible coordination structure of WN<sub>4</sub>, W-N<sub>2</sub>C<sub>2</sub>-a, W-N<sub>2</sub>C<sub>2</sub>-b, W-N<sub>3</sub>C<sub>1</sub>, which implied its remarkable alkaline HER performance ( $\eta_{10}$ : 85 mV in 0.1 M KOH) [67]. To expand the multifunctional active materials scaled-up synthesis methods, Lai et al. constructed a bifunctional electrocatalyst with dual active sites (Ir@NC<sub>3</sub> for HER, Ir@Co(Ir) for OER), i.e., Ir single atoms loaded onto Co-embedded N-doped carbon nanostructures that can simultaneously accelerate both the HER and the OER, as shown in Figure 3d [68]. Jin et al., constructing the Pt SACs comprising the Pt-N<sub>2</sub>C<sub>2</sub> active sites using ball milling comprising a mixed precursor of nitrogen-doped carbon spherical NPs and K<sub>2</sub>PtCl<sub>4</sub> powder [69]. Further, the Mo single atom was stabilized over porous nitrogen-doped mesopores carbon, constructing a Mo<sub>1</sub>N<sub>1</sub>C<sub>2</sub> local structure and showing a superior activity compared to Mo<sub>2</sub>C and MoN [70].

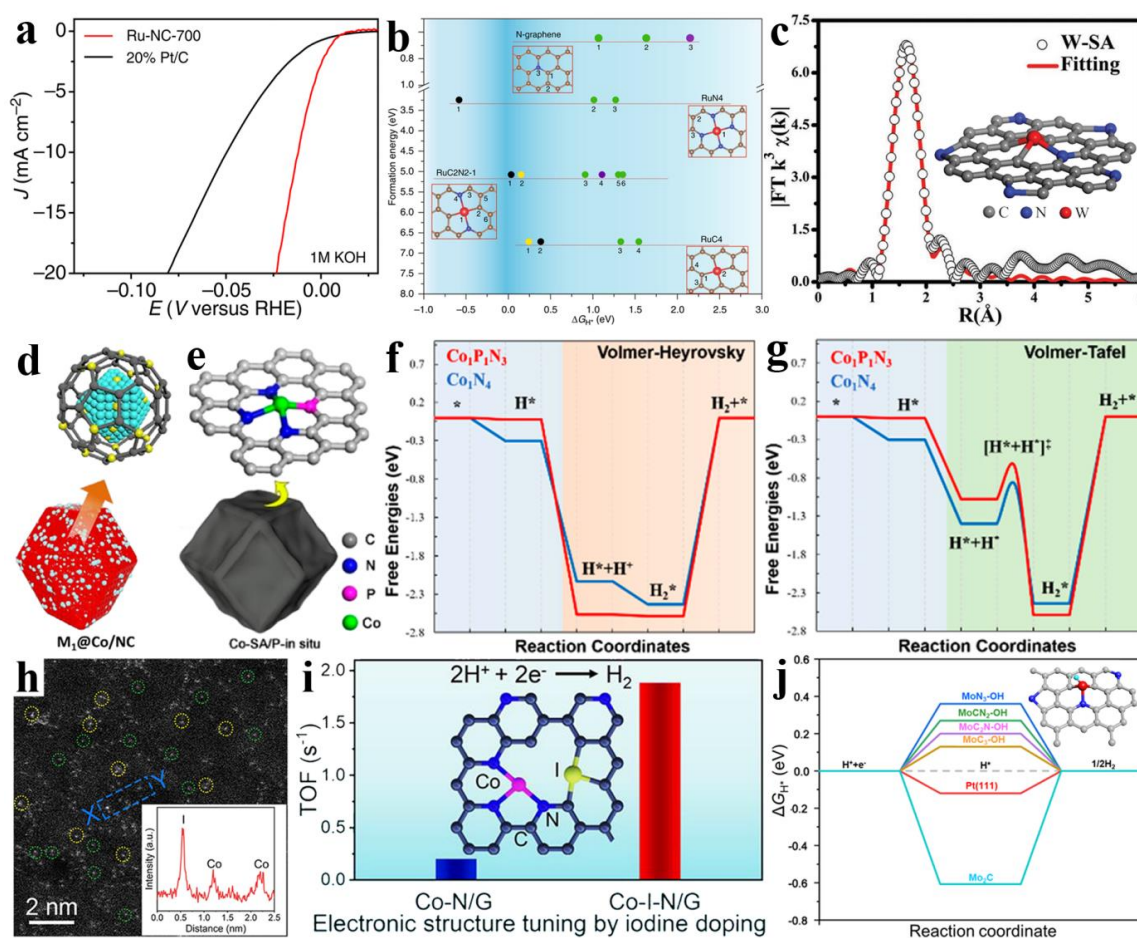


**Figure 3.** (a) LSV curves. (b) Free energy diagram of the different RuC<sub>x</sub>N<sub>y</sub> structures. Reprinted with permission from ref. [66]. Copyright (2019) Nature Publishing Group. (c)  $k^3$ -weight FT-EXAFS fitting

curves of the W–SAC at W  $L_3$ –edge. Reprinted with permission from ref. [67]. Copyright (2018) Wiley–VCH Verlag GmbH & Co. KGaA, Weinheim. (d) Schematic of the formation for  $M_1@Co/NC$ . Reprinted with permission from ref. [68]. Copyright (2019) Wiley–VCH Verlag GmbH & Co. KGaA, Weinheim. (e) Scheme of the formation for Co–SA/P–in situ. Free energy diagrams of (f) the Volmer–Heyrovsky step and (g) the Volmer–Tafel step of the HER. Reprinted with permission from ref. [71]. Copyright (2020) American Chemical Society. (h) Atomic–scale HAADF–STEM images of Co–I–N/G. (i) Schematic illustration of the electronic construction. Reprinted with permission from ref. [72]. Copyright (2021) American Chemical Society. (j) Free energy profile of Mo–SACs and Pt (111) (inset, the hydrogenated  $MoC_2N-OH$ ). Reprinted with permission from ref. [73]. Copyright (2021) American Chemical Society. \* represents the active site.

Replacing the N/C atoms in  $MN_xC_y$  with other species of a weaker electronegativity, e.g., P and B, can also regulate the local environment of the metal atom centers. Wang et al. applied an in situ phosphatizing strategy—a direct pyrolysis treatment of triphenylphosphine encapsulated within ZIF–67—to obtain an atomic  $Co_1-P_1N_3$  interfacial structure that was denoted as Co–SA/P (Figure 3e) with a  $\eta_{10}$  of 98 mV in 0.5 M  $H_2SO_4$ . They discovered that a key factor for enhancing the activity was a bond length extending high–valent  $Co_1-P_1N_3$  interfacial configuration (Figure 3f,g) [71]. Meanwhile, according to the DFT calculation, the  $sp$ – and  $sp^2$ –hybridized B species–doped Co@GY (Co@ $B_2-GY$ ) material was found to boast an exceptional activity for the HER as well [74]. The iodine (I) species, with 2.66 electronegativities, were distinct from B (2.04), S (2.58), and P (2.19), and thus were endowed with several distinguishing features. Liu et al. synthesized a cobalt–nitrogen–carbon (Co–N–C) sample, whose interior had an I–doped carbon matrix with low–coordinated  $CoN_3$  and  $IN_3$  sites. These sites needed to be anchored at the edge or defect within the graphene since the I was difficult to replace and dope onto the carbon lattice due to its high atomic radius (Figure 3h,i). The incorporation of the iodine heteroatoms not only enhanced the catalyst’s specific surface area but also lowered the chemical oxidation state of the Co sites, ultimately optimizing the hydrogen adsorption and enhancing its HER kinetics ( $\eta_{10}$ : 85 mV in 0.5 M  $H_2SO_4$ ) [72]. In an asymmetric axial coordination structure, Li et al. prepared a configuration of a N/C/O triple–coordinated Mo atom site with an additional axial O atom (Mo– $O_1N_1C_2$ ). The coordination of the nonmetallic atoms, e.g., C, N, and O, dramatically modulated the Mo centers’ electronic reconfiguration at the atomic scale, and the rich local microenvironment imparted a beneficial  $H^*$  adsorption energy to the formed Mo– $O_1N_1C_2$ , thus enhancing its inherent activity (Figure 3j). Note that for the reduction potential of the acidic media, the dangling O was readily hydrogenated to form hydroxyls, and the obtained  $MoC_2N-OH$  local structure might have been a prospective catalytic center for the HER ( $\eta_{10}$ : 66 mV in 0.5 M  $H_2SO_4$ ) [73].

The incorporation of extra nonmetallic atoms in the carbon–based supports to boost the activity of the catalytic sites for the HER has become a versatile strategy. In particular, the doped species with a different electronegativity from C, mainly N, S, P, B, O, I, Cl, etc., can be doped onto different coordination shells or even in the axial space. As one of the highly electronegative atoms, N is often combined into carbon–based carriers together with other heteroatoms to form non–traditional  $M-N_x-O/S/P/B/Cl/I$  structure catalysts.

### 3.3. Dual–Metal Coordination Structure

Bimetallic heteroatomic coordination, i.e., diatomic catalysts, as an extension of the SACs, have higher metal loads and complex and flexible center site configurations, and afford more electrocatalytic possibilities, and thus have received much attention recently. They can be classified as direct bimetallic interbonds ( $M_1-M_2$ ) or indirect bridging oxygen bonds ( $M_1-O-M_2$ ) according to the difference in the bimetallic center connection.

Zhou et al. designed an Rh–Fe interbonding promoter that can disperse Fe NPs into the corresponding Fe atoms at low temperatures (FR–NCS). The theoretical calculations also revealed that the Fe cluster– $Fe-N_4$  intermediate, which causes the neighboring carbon vacancies to trap the moving Rh atoms, as shown in Figure 4a, b, is the source of the atomic

dispersion process. The Rh/Fe bond substantially aids in the thermodynamic stability at an atomic level and results in the FR–NCS exhibiting a higher HER activity ( $\eta_{10}$ : 22 mV in 0.5 M H<sub>2</sub>SO<sub>4</sub>) than the commercial Pt/C, as shown in Figure 4c [75]. Zhang et al. used a more precise atomic layer deposition (ALD) technique to selectively form the diatomic sites by carefully controlling the deposition conditions, so that the next Ru could only attach to the primary Pt to construct high–quality Pt–Ru dimer structures on the nitrogen–doped carbon nanotubes. According to calculation results, the Pt atoms had a significant impact on the Ru sites' electronic distribution and also modified the original inertness between H and Ru through the synergistic effects of the Pt–Ru dimer, which boosted the HER activity [76]. Further, Hu et al. reported a special bimetallic site that coexisted with the NPs, i.e., part of the single atom (FeN<sub>4</sub>, RuN<sub>4</sub>) and part of the nanoparticle (Ru NPs)–loaded Fe/N co–doped carbon support via a coupling of an Ru atom and Ru NPs (inset of Figure 4d). In the synthesis, the Fe–N<sub>4</sub> moieties diffused larger Ru NPs into smaller Ru clusters, even the atomically dispersed Ru–N<sub>4</sub>. In the hydrogen evolution, the FeN<sub>4</sub> groups effectively modulated the electron distribution of the smaller Ru clusters, and Ru–N<sub>4</sub> partially promoted the splitting of the H<sub>2</sub>O molecules, intermediated their generation, and then recombined them into H<sub>2</sub> molecules on the nearby modulated Ru cluster, as shown in Figure 4d,e. In other words, they synergistically improved the HER performance under alkaline conditions ( $\eta_{10}$ : 9 mV in 1 M KOH), as shown in Figure 4f [77]. For the bridging oxygen bimetallic coordination, Yu et al. accurately bridged the oxygen molecules to graft a single–atom Pt onto another Fe atom site, forming Pt<sub>1</sub>@Fe–N–C catalysts with novel Pt<sub>1</sub>–O<sub>2</sub>–Fe<sub>1</sub>–N<sub>4</sub> groups and obtaining a high Pt loading of 2.1wt% (Figure 4g). The DFT calculations confirmed that Pt<sub>1</sub>@Fe–N–C possesses better H\* adsorption–desorption properties, accounting for the high active grafting bond of the Pt<sub>1</sub>–O<sub>2</sub>–group (Figure 4h) and exhibited an unexpected performance close to 20% Pt/C ( $\eta_{10}$ : 60 mV in 0.5 M H<sub>2</sub>SO<sub>4</sub>) [78]. Moreover, Yang et al. designed a similar O–bridged W–Mo dual atom structure catalyst (W<sub>1</sub>Mo<sub>1</sub>–NG DAC), as shown in Figure 4i, through a self–assembling and a subsequent nitrogenation procedure. The synthesized O–bridged W–O–Mo–O–C local structure was anchored to the N–doped graphene vacancies, and the electron delocalization effect of this configuration provided the optimized H\* adsorption strength. Thus, the synthesized W<sub>1</sub>Mo<sub>1</sub>–NG DAC achieved a Pt–like catalytic activity and an ultra–high durability for the HER ( $\eta_{10}$ : 24 mV in 0.5 M H<sub>2</sub>SO<sub>4</sub>;  $\eta_{10}$ : 67 mV in 1 M KOH) in the common electrolytes with a wide pH [79].

According to the aforementioned reports, it was noted that one metal species can encourage the dispersion of the other species and increase their thermodynamic durability. In the catalytic process, the bimetallic site catalysts have a unique advantage in their synergistic effect, which makes them superior to the SACs in modulating the adsorption state toward the hydrogen intermediates and reducing the reaction energy barrier of the reaction steps for the HER.

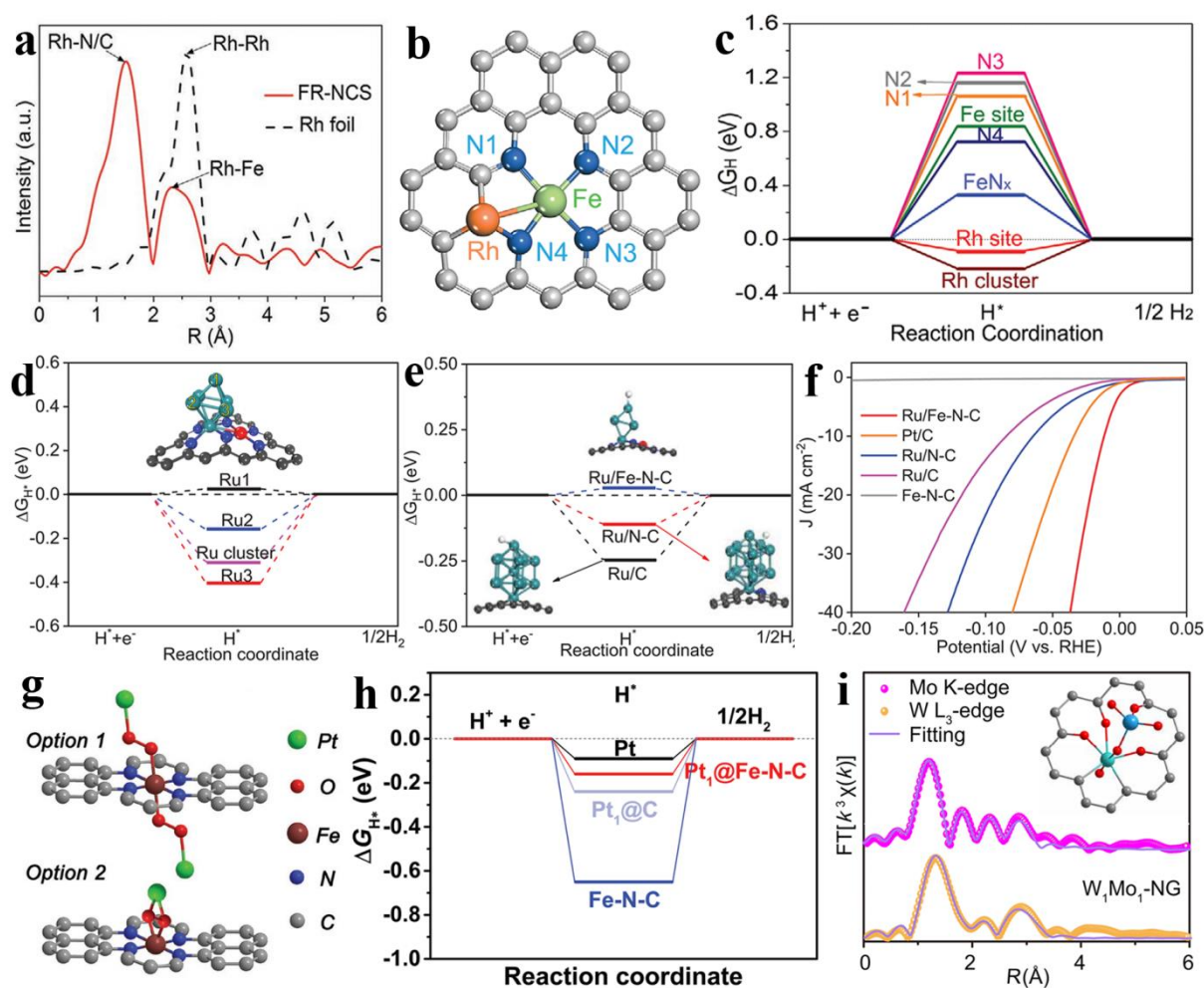


**Figure 4.** (a) FT-EXAFS data of Rh in the FR-NCS. (b) Possible sites to adsorb H. (c)  $\Delta G_{H^*}$  of the different sites. Reprinted with permission from ref. [75]. Copyright (2020) Wiley-VCH GmbH. (d)  $\Delta G_{H^*}$  of the possible sites toward the Ru/Fe-N-C system. (e) Comparison of the  $\Delta G_{H^*}$  of the HER. (f) LSV curves. Reprinted with permission from ref. [77]. Copyright (2020) The Authors. Advanced Science published by Wiley-VCH GmbH. (g) Schematic diagram of Pt<sub>1</sub>-O<sub>2</sub>-Fe<sub>1</sub>-N<sub>4</sub>-C<sub>12</sub> as the active moiety of Pt<sub>1</sub>@Fe-N-C. (h) Calculated  $\Delta G_{H^*}$ . Reprinted with permission from ref. [78]. Copyright (2017) Wiley-VCH Verlag GmbH & Co. KGaA, Weinheim. (i) Mo K-edge and W L<sub>3</sub>-edge EXAFS fitting curves for W<sub>1</sub>Mo<sub>1</sub>-NG at the R-space and k-space, respectively. Reprinted with permission from ref. [79]. Copyright (2020) The Authors, some rights reserved; exclusive licensee of the American Association for the Advancement of Science.

### 3.4. Asymmetric Atom Sites of Organic/Metal-based Supports for HER

Due to the original MOFs' instability or poor conductivity under alkaline and acidic conditions, which limited them from acting as electrocatalysts for the HER, researchers have designed the structures of the MOFs or combined them with other substrates with better conductivity.

Huang et al. designed bimetallic site MOFs (M<sub>2</sub>(M<sub>1</sub><sub>3</sub>-HAHATN)<sub>2</sub>) with extra M-N<sub>2</sub> moieties by employing hexaiminohexaazatrinaphthalene (HAHATN) to serve as a conjugated ligand, as shown in Figure 5a,b. The optimal Ni<sub>3</sub>(Ni<sub>3</sub>-HAHATN)<sub>2</sub> nanosheets possessed a satisfactory  $\eta_{10}$  of 115 mV and a Tafel slope of 45.6 mV dec<sup>-1</sup> in 0.1 M KOH. Both the theoretical and experimental data indicated that the metal atoms on the excess M-N<sub>2</sub> group had a higher unsaturation in comparison to those on the M-N<sub>4</sub> sites, for promoting the donation of electrons and enhancing the catalytic activity (Figure 5c) [80]. Meanwhile, Wu et al. reported two novel Co-MOFs (CTGU-5 and -6), which could be

selectively crystallized to other new two-dimensional (2D) or three-dimensional (3D) nets by changing the anionic or neutral surfactants (Figure 5d,f). As shown in Figure 5e,g, the coordination model of the H<sub>2</sub>O molecules, which is a key structural distinction between CTGU-5 and CTGU-6, differed significantly. The H<sub>2</sub>O was coordinated to the Co site in CTGU-5, whereas in CTGU-6, the H<sub>2</sub>O was a lattice molecule of the framework through a hydrogen bond. This difference produced two distinct crystal structures, which in turn, influenced the electrocatalytic characteristics of the HER. The composite composed of CTGU-5(1:4) and acetylene black (AB) was determined to have the highest HER performance ( $\eta_{10}$ : 388 mV in 0.5 M H<sub>2</sub>SO<sub>4</sub>) of all the MOFs after systematically altering the ratio of the two materials [81]. Moreover, Lin et al. created binderless FeNi(BDC)(DMF,F)/NF polymer electrodes by using a nickel foam surface to grow the bimetallic MOFs compounds in situ, which were fully modulated by alloying Ni and Fe, where each contained two molecularly well-combined metal nanoclusters and delivered 10 and 400 mA cm<sup>-2</sup> current densities at the ultra-low applied potentials of 1.58 and 1.90 V, respectively. This superior activity might be owed to the intra-molecular synergism between the FeO<sub>6</sub> and NiO<sub>6</sub> clusters [82]. Another reported crystalline composition, i.e., a two novel polyoxometalates (POM)-encapsulated metal-organic nanotube (HUST-200, HUST-201), can serve as stable and highly effective HER electrocatalysts [83]. For the metal-based supports, in 2017, Chao et al. designed a Cu-Pt two-site alloy with Pd nanorings (Pd/Cu-Pt NRs), which underwent a two-step approach composed of sequentially reacting the Cu- and Pt-based solutions with the Pd nanorings solutions. The FT-EXAFS measurement confirmed the appearance of the Cu-Pt coordination with a 2.67 Å bond length (Figure 5h). The synthesized novel Pd/Cu-Pt NRs can greatly boost the HER ( $\eta_{10}$ : 22.8 mV in 0.5 M H<sub>2</sub>SO<sub>4</sub>), as shown in Figure 5k, based on the theoretical calculation and experimental results, and the higher activity may originate from the Cu-Pt double atom sites (Figure 5i,j) [84].

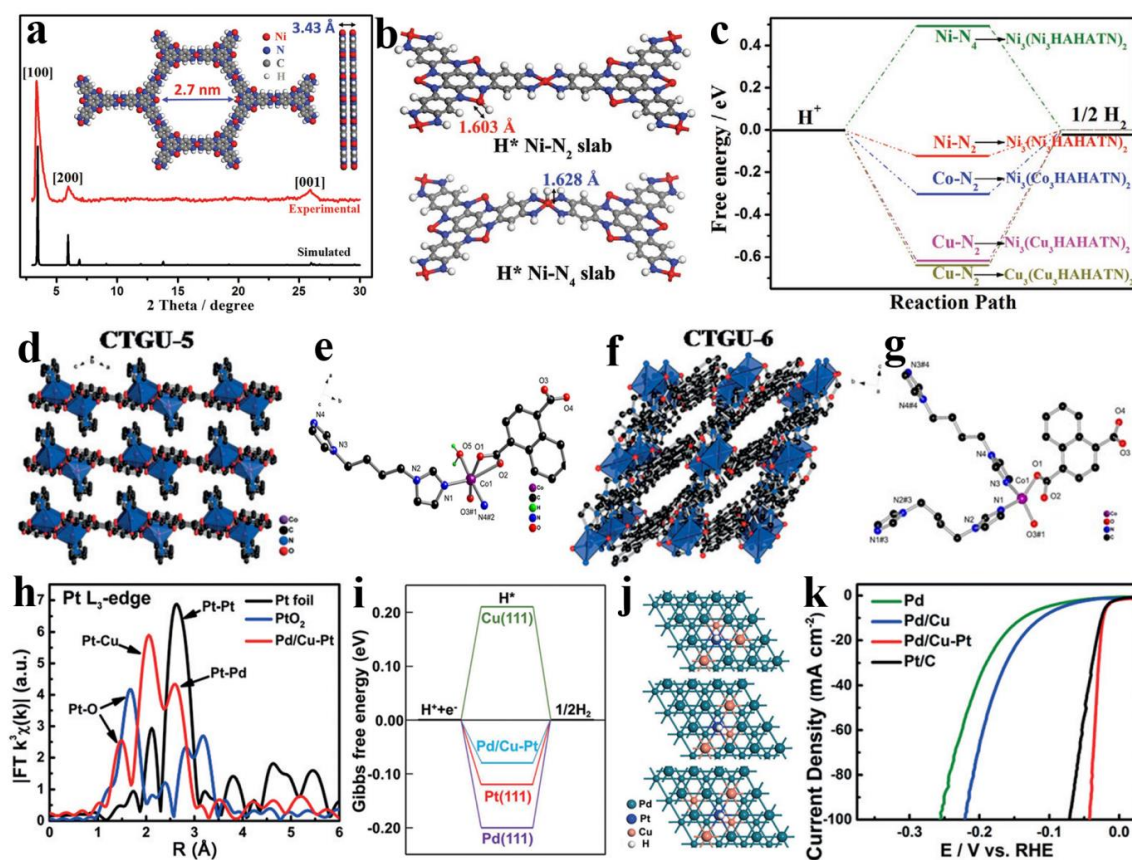


**Figure 5.** (a) Experimental and simulated PXRD patterns of Ni<sub>3</sub>(Ni<sub>3</sub>-HAHATN)<sub>2</sub>. (b) Hydrogen adsorption slabs. (c) Free energy profiles for the HER over the electrocatalytic sites. Reprinted with

permission from ref. [80]. Copyright (2020) The Authors. Published by Wiley–VCH Verlag GmbH & Co. KGaA, Weinheim. The crystal structure diagrams and the corresponding asymmetric unit for (d,e) CTGU–5 and (f,g) CTGU–6. Reprinted with permission from ref. [81]. Copyright (2017) Wiley–VCH Verlag GmbH & Co. KGaA, Weinheim. (h)  $k^3$ –weighted  $\chi(k)$ –function of the EXAFS spectra for the Pt  $L_3$ –edge. (i) The free energy diagram. (j) Models for the Pd/Cu–Pt NRs. (k) LSV curves. Reprinted with permission from ref. [84]. Copyright (2017) Wiley–VCH Verlag GmbH & Co. KGaA, Weinheim.

MOF materials are often used as precursors to obtain catalysts with atomically dispersed products, while the direct use of the MOF as the HER electrocatalysis for the hydrogen evolution is less reported. The majority of the catalytic activities toward the MOF are hardly similar to those of the materials composed of carbon and metal. However, the well–defined metal nodes with a coordination environment and a customizable structure of the MOF can be an ideal platform to study the catalytic activity centers.

#### 4. Summary and Outlook

The SACs catalyst with an asymmetric local coordination and a flexible adjustment of the coordination configuration was rapidly expended in the HER catalysis as compared to the traditional  $M-N_4$  sites, which resulted from their unique electronic and geometric structure (Table 1).

**Table 1.** The comparison of the HER performance of the carbon–based SACs with the different active sites.

Catalyst	Active Site	Electrolyte	Current Density ( $\text{mA cm}^{-2}$ ), Overpotential (mV)	Stability	Ref.
E–Co SAs	$\text{CoN}_2$	1 M KOH	10, ~59	$500 \text{ mA cm}^{-2}$ , 200 h	[59]
Co $\text{N}_4$	$\text{CoN}_4$	1 M KOH	10, ~150	–	
Co $_1$ /PCN	$\text{CoN}_4$	1 M KOH	10, 89	$10 \text{ mA cm}^{-2}$ , 24 h	[85]
Co $\text{N}_x$ /C	$\text{CoN}_4$	1 M KOH	10, 170	–	[86]
	$\text{CoN}_4$	0.5 M $\text{H}_2\text{SO}_4$	10, 133	LSVs, 5000 cycles	
Co–NG–MW	$\text{CoN}_4$	0.5 M $\text{H}_2\text{SO}_4$	10, 127	LSVs, 1000 cycles	[87]
Co–SA–without P	$\text{CoN}_4$	0.5 M $\text{H}_2\text{SO}_4$	10, 148	–	[71]
Co–SA/P–in situ	$\text{CoP}_1\text{N}_3$	0.5 M $\text{H}_2\text{SO}_4$	10, 98	LSVs, 1000 cycles	[71]
Pt@PCM	$\text{PtN}_4$	0.5 M $\text{H}_2\text{SO}_4$	10, 105	$\sim 22.5 \text{ mA cm}^{-2}$ , 5 h	[88]
Pt SACs/AG	$\text{PtN}_4$	0.5 M $\text{H}_2\text{SO}_4$	10, 12	LSVs, 2000 cycles	[89]
$\text{Pt}_1$ /NPC	$\text{PtN}_4$	0.5 M $\text{H}_2\text{SO}_4$	10, 25	LSVs, 3000 cycles	[90]
$\text{Pt}_1$ /MC	$\text{PtC}_3$	0.5 M $\text{H}_2\text{SO}_4$	10, ~27	LSVs, 1000 cycles	[63]
Pt@NC–B	$\text{PtN}_2\text{C}_2$	0.5 M $\text{H}_2\text{SO}_4$	10, 39	$10 \text{ mA cm}^{-2}$ , 40 h	[69]
$\text{Pt}_1$ /OLC	$\text{PtO}_2\text{C}_1$	0.5 M $\text{H}_2\text{SO}_4$	10, ~38	$10 \text{ mA cm}^{-2}$ , 100 h	[91]
Ru–NC–700	$\text{RuC}_2\text{N}_2$	1 M KOH	10, 12	LSVs, 10,000 cycles	[66]
$\text{Ru}_1$ /N–C	$\text{RuN}_4$	1 M KOH	10, 173	–	[92]
	$\text{RuN}_4$	0.5 M $\text{H}_2\text{SO}_4$	10, 282	–	
Ru SAs@PN	$\text{RuN}_4$	0.5 M $\text{H}_2\text{SO}_4$	10, 24	LSVs, 5000 cycles	[93]
Ni–SA/NC	$\text{NiN}_3$	1 M KOH	10, 102	LSVs, 5000 cycles	[58]
Ni–N–C	$\text{NiN}_4$	1 M KOH	10, 307	–	[94]
$\text{Ni}_{\text{sub}}$ /G	$\text{NiC}_3$	0.5 M $\text{H}_2\text{SO}_4$	10, ~50	$\sim 9 \text{ mA cm}^{-2}$ , 120 h	[61]
W–SA	$\text{WN}_1\text{C}_3$	0.1 M KOH	10, 85	LSVs, 10,000 cycles	[67]
$\text{Mo}_1\text{N}_1\text{C}_2$	$\text{MoN}_1\text{C}_2$	0.1 M KOH	10, 132	LSVs, 1000 cycles	[70]
Mo@NMCNFs	$\text{MoN}_1\text{C}_2\text{–O}_1$	0.5 M $\text{H}_2\text{SO}_4$	10, 66	LSVs, 3000 cycles	[73]
FR–NCS	$\text{Rh–FeN}_4$	0.5 M $\text{H}_2\text{SO}_4$	10, 22	LSVs, 1000 cycles	[75]
$\text{Pt}_1$ @Fe–N–C	$\text{Pt–O}_2\text{–FeN}_4$	0.5 M $\text{H}_2\text{SO}_4$	10, 60	$5 \text{ mA cm}^{-2}$ , 5.5 h	[78]
$\text{W}_1\text{Mo}_1$ –NG	W–O–Mo–O–C	0.5 M $\text{H}_2\text{SO}_4$	10, 24	$10 \text{ mA cm}^{-2}$ , 100,000 s	[79]
		1 M KOH	10, 67	$10 \text{ mA cm}^{-2}$ , 100,000 s	

In order to compare the differences in the HER properties between the symmetric and asymmetric atomic sites, two elements–Co and Pt–were selected as the representatives of the non–precious and precious metal atomic catalysts for the investigation (Figure 6). In the Co–based SACs, it was discovered that a low–coordination  $\text{CoN}_2$  active site demonstrated a greater HER performance than the symmetric coordination  $\text{CoN}_4$  moieties in the 1 M KOH alkaline electrolytes. This finding remains consistent in the 0.5 M  $\text{H}_2\text{SO}_4$  solutions,

i.e., the heteroatom–coordination  $\text{CoP}_1\text{N}_3$  center was superior to the traditional  $\text{CoN}_4$  sites. Nevertheless, the variations in the HER performance of the symmetric/asymmetric Pt sites were not considerable, and some prominent features should not be neglected for the asymmetric sites. Consequently, when designing and creating atomic catalysts, the origin of the catalytic active component (metal atom center and nearby coordination atoms) and the modulation of the activity (electronic structure of the central single atom and its interaction with the support) are the two wider aspects that must be considered [95–99]. Moreover, from reviewing and examining the employment of the asymmetric atom electrocatalysts in the HER, it is evident that some new discoveries and insights have been made in the structural design of the asymmetric atomic catalysts for the HER, which can be briefly summarized in the following, hoping to provide some instructions for the design of the HER catalyst at the atomic level [100–103].

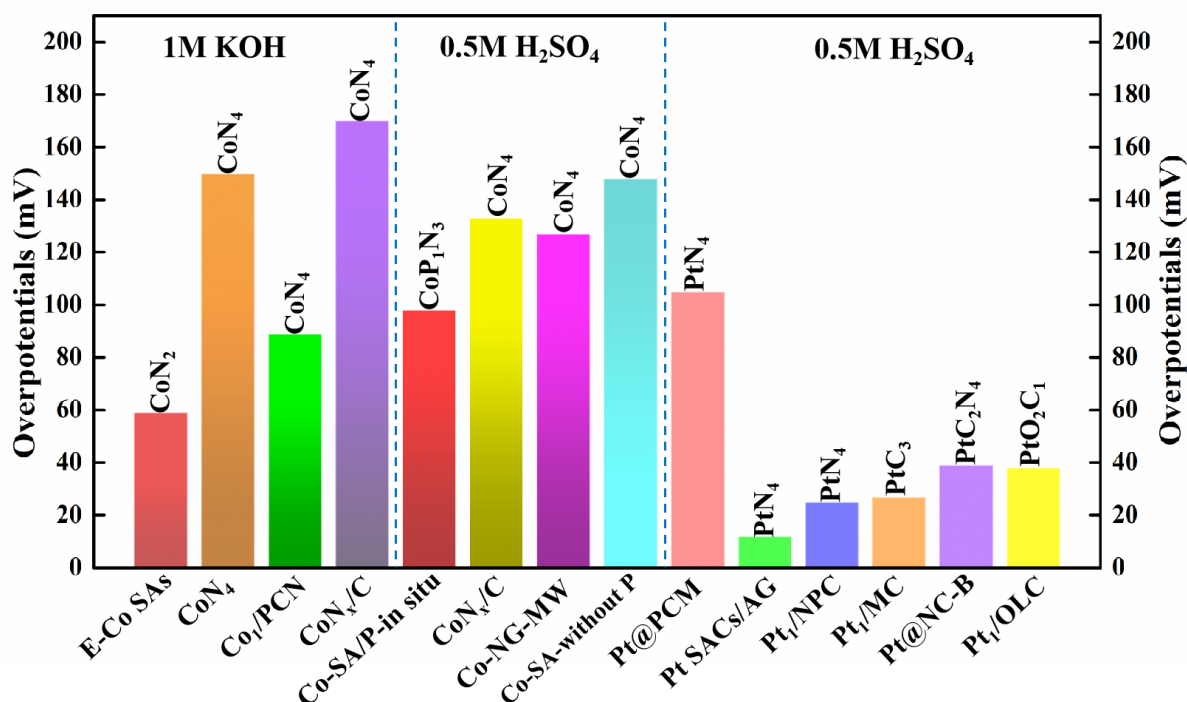


**Figure 6.** The HER performance overviews of the symmetric/asymmetric coordination sites.

(i) Among these low–coordination asymmetric sites,  $\text{NiN}_3$  and  $\text{CoN}_2$  are commonly used in SACs and possess a better HER performance, which may arise from the differences in the electrolyte environment and the material microstructure [104–107]. Both noble and non–precious metals are involved in the HER, and by comparing the reported experimental data, the carbon coordination seems to be better than N coordination. (ii) In the published lateral/axial coordination works for the HER, the species of the heteroatoms are numerous, consisting of C, N, O, P, B, and I, etc. [108–113]. The representative metal centers for the HER are Pt, Ru, Ir, Mo, Co, and W. As can be observed, compared to the coordination environment, the role of the metal–centered species is crucial. (iii) For the diatomic HER, except for Mo, W, and Fe, noble metals (Pt, Ru, Rh) are predominantly present. For the coordination mode, compared to the monotonous  $\text{M}_2\text{N}_6$ , there are more types of HER, e.g., the bridged  $\text{M-O-M}$ , which can offer some new ideas for the structural design of SACs [114–119]. (iv) The comparison of the above–mentioned data reveals that the asymmetric coordination of the organic supports seems to have poorer results than the carbon supports. Except for the variation in the coordination environment, the metal species include precious metals or transition metals, however the reports on the metal supports are few [120–124].

Hydrogen, a widespread element in nature, is perceived as being one of the most hopeful renewable energy substitutes. To minimize the barrier of H<sub>2</sub>O electrolysis, SACs are adopted as effective and inexpensive catalysts, whose catalytic features are often determined by the metal center sites and the local coordination atoms that come from the support, demonstrating various characteristics such as higher activity and more ideal selectivity. In the design of the atomic configuration, the asymmetric coordination structure exhibits a more flexible combination of manners, e.g., through spatial structure optimization and electron transfer, the bond strength of the reactants/intermediates on the catalytic site can be optimized to balance the energy barriers, thus accelerating the overall reaction rate [125–130]. Moreover, we present the remaining challenges and the expected directions of the asymmetric atomic catalysts for hydrogen production from water splitting.

(i) Advanced atomic structural characterization. The precise determination of the coordination structure over the atomic resolution is a significant matter for a comprehensive knowledge of the evolution of SACs. The interpretation of the coordination atoms/types on the central sites is still challenging, even with the most widely used characterization methods, such as FTIR spectra, XPS, XAFS, and HAADF–STEM, etc. [131–134]. For example, XAFS has difficulty distinguishing between the various coordination atoms with close atomic numbers (Z) and/or similar bond distances [135–138]. The HAADF–STEM also has difficulty in identifying the active atoms when their Z–values are close to those of the support [139–142]. Impressively, several in situ/operando characterization strategies enable us to unravel the evolution of the coordination environment and elucidate the catalytic mechanism during the reaction process.

(ii) Long–term stability. In comparison to conventional catalysts, SACs are more sensitive to the surrounding conditions and more prone to degradation during storage or application, especially when operating in highly corrosive electrolytes with large current densities. In terms of the HER, the numerous reports of SACs perform on par with or even better than commercial Pt, but their long–term durability poses a significant obstacle to their practical implementation in industrial hydrogen production, as they must generally retain their activity and stability for longer than 1000 h [143–146].

(iii) Scale–up production. Controlled and streamlined methods are needed to generate asymmetric SACs with high activity that meet the requirements of continuous and large–scale production. It should be noted that the presence of symmetric atoms, nanoclusters, and nanoparticles is difficult to avoid in the preparation of asymmetric atomic catalysts, and thus more attention should be paid to the quality of the finished catalyst. Furthermore, increasing the atomic loading is an efficacious strategy for further boosting the mass activity of the SACs. However, the present reported atom loading is limited to ~10 wt%, for which this still needs more effort [147–150].

**Funding:** This work was financially supported by the National Natural Science Foundation of China (22075211, 21601136, 51971157, and 22275166) and the Tianjin Science Fund for Distinguished Young Scholars (19JCJQC61800).

**Conflicts of Interest:** The authors declare no conflict of interest.

## References

1. Wang, L.; Wang, D.; Li, Y. Single-atom catalysis for carbon neutrality. *Carbon Energy* **2022**, *4*, 1021–1079. [[CrossRef](#)]
2. Posada-Pérez, S.; Vidal-Lopez, A.; Solà, M.; Poater, A. 2D Carbon Nitride as Support of Single Cu, Ag, and Au Atoms for Carbon Dioxide Reduction Reaction. *Phys. Chem. Chem. Phys.* **2023**. [[CrossRef](#)]
3. Gao, S.; Chen, S.; Liu, Q.; Zhang, S.; Qi, G.; Luo, J.; Liu, X. Bifunctional BiPd Alloy Particles Anchored on Carbon Matrix for Reversible Zn-CO<sub>2</sub> Battery. *ACS Appl. Nano Mater.* **2022**, *5*, 12387–12394. [[CrossRef](#)]
4. Musah, J.-D.; Ilyas, A.M.; Venkatesh, S.; Mensah, S.; Kwofie, S.; Roy, V.A.L.; Wu, C.-M.L. Isovalent substitution in metal chalcogenide materials for improving thermoelectric power generation-A critical review. *Nano Res. Energy* **2022**, *1*, 9120034. [[CrossRef](#)]
5. Huhta, K. The contribution of energy law to the energy transition and energy research. *Glob. Environ. Chang.* **2022**, *73*, 102454. [[CrossRef](#)]

6. Qi, D.; Lv, F.; Wei, T.; Jin, M.; Meng, G.; Zhang, S.; Liu, Q.; Liu, W.; Ma, D.; Hamdy, M.S.; et al. High-efficiency electrocatalytic NO reduction to NH<sub>3</sub> by nanoporous VN. *Nano Res. Energy* **2022**, *1*, e9120022. [[CrossRef](#)]
7. Payandeh, S.; Strauss, F.; Mazilkin, A.; Kondrakov, A.; Brezesinski, T. Tailoring the LiNbO<sub>3</sub> coating of Ni-rich cathode materials for stable and high-performance all-solid-state batteries. *Nano Res. Energy* **2022**, *1*, e9120016. [[CrossRef](#)]
8. Liu, J.; Huang, Z.; Fan, M.; Yang, J.; Xiao, J.; Wang, Y. Future energy infrastructure, energy platform and energy storage. *Nano Energy* **2022**, *104*, 107915. [[CrossRef](#)]
9. Gao, X.; Li, J.; Zuo, Z. Advanced electrochemical energy storage and conversion on graphdiyne interface. *Nano Res. Energy* **2022**, *1*, 9120036. [[CrossRef](#)]
10. Zhang, Q.; Zhang, S.; Luo, Y.; Liu, Q.; Luo, J.; Chu, P.; Liu, X. Preparation of high entropy alloys and application to catalytical water electrolysis. *APL Mater.* **2022**, *10*, 070701. [[CrossRef](#)]
11. Wang, W.; Hong, X.; Yao, Q.; Lu, Z.-H. Bimetallic Ni-Pt nanoparticles immobilized on mesoporous N-doped carbon as a highly efficient catalyst for complete hydrogen evolution from hydrazine borane. *J. Mater. Chem. A* **2020**, *8*, 13694–13701. [[CrossRef](#)]
12. Wang, D.; Yang, P.; Liu, L.; Wang, W.; Chen, Z. Atomically dispersed metal-nitrogen-carbon electrocatalysts for oxygen reduction reaction: From synthesis strategies to activity engineering. *Mater. Today Energy* **2022**, *26*, 101017. [[CrossRef](#)]
13. Wyvratt, B.M.; Gaudet, J.R.; Pardue, D.B.; Marton, A.; Rudić, S.; Mader, E.A.; Cundari, T.R.; Mayer, J.M.; Thompson, L.T. Reactivity of Hydrogen on and in Nanostructured Molybdenum Nitride: Crotonaldehyde Hydrogenation. *ACS Catal.* **2016**, *6*, 5797–5806. [[CrossRef](#)]
14. Liu, Q.; Hu, Y.; Yu, X.; Qin, Y.; Meng, T.; Hu, X. The pursuit of commercial silicon-based microparticle anodes for advanced lithium-ion batteries: A review. *Nano Res. Energy* **2022**, *1*, 9120037. [[CrossRef](#)]
15. Zhang, Y.; Yang, J.; Ge, R.; Zhang, J.; Cairney, J.M.; Li, Y.; Zhu, M.; Li, S.; Li, W. The effect of coordination environment on the activity and selectivity of single-atom catalysts. *Coord. Chem. Rev.* **2022**, *461*, 214493. [[CrossRef](#)]
16. Su, H.; Soldatov, M.A.; Roldugin, V.; Liu, Q. Platinum single-atom catalyst with self-adjustable valence state for large-current-density acidic water oxidation. *eScience* **2022**, *2*, 102–109. [[CrossRef](#)]
17. Liu, W.; Feng, J.; Wei, T.; Liu, Q.; Zhang, S.; Luo, Y.; Luo, J.; Liu, X. Active-site and interface engineering of cathode materials for aqueous Zn-gas batteries. *Nano Res.* **2023**, *16*, 2325–2346. [[CrossRef](#)]
18. Chen, F.; Jiang, X.; Zhang, L.; Lang, R.; Qiao, B. Single-atom catalysis: Bridging the homo- and heterogeneous catalysis. *Chin. J. Catal.* **2018**, *39*, 893–898. [[CrossRef](#)]
19. Zhang, H.; Wei, T.; Qiu, Y.; Zhang, S.; Liu, Q.; Hu, G.; Luo, J.; Liu, X. Recent Progress in Metal Phosphorous Chalcogenides: Potential High-Performance Electrocatalysts. *Small* **2023**. [[CrossRef](#)] [[PubMed](#)]
20. Liang, Y.; Wei, J.; Qiu, X.; Jiao, N. Homogeneous Oxygenase Catalysis. *Chem. Rev.* **2018**, *118*, 4912–4945. [[CrossRef](#)] [[PubMed](#)]
21. Cornils, B. Catalysis. Concepts and Green Applications. By Gadi Rothenberg. *Angew. Chem. Int. Ed.* **2008**, *47*, 5500–5501. [[CrossRef](#)]
22. Sun, Z.; Wen, X.; Wang, L.; Ji, D.; Qin, X.; Yu, J.; Ramakrishna, S. Emerging design principles, materials, and applications for moisture-enabled electric generation. *eScience* **2022**, *2*, 32–46. [[CrossRef](#)]
23. Zhang, H.; Qiu, Y.; Zhang, S.S.; Liu, Q.; Luo, J.; Liu, X.J. Nitrogen-incorporated iron phosphosulfide nanosheets as efficient bifunctional electrocatalysts for energy-saving hydrogen evolution. *Ionics* **2022**, *28*, 3927–3934. [[CrossRef](#)]
24. Rozzi, E.; Minuto, F.D.; Lanzini, A.; Leone, P. Green Synthetic Fuels: Renewable Routes for the Conversion of Non-Fossil Feedstocks into Gaseous Fuels and Their End Uses. *Energies* **2020**, *13*, 420. [[CrossRef](#)]
25. Zhang, H.; Luo, Y.; Chu, P.; Liu, Q.; Liu, X.; Zhang, S.; Luo, J.; Wang, X.; Hu, G. Recent advances in non-noble metal-based bifunctional electrocatalysts for overall seawater splitting. *J. Alloy. Compd.* **2022**, *922*, 166113. [[CrossRef](#)]
26. Heppe, N.; Gallenkamp, C.; Paul, S.; Segura-Salas, N.; von Rhein, N.; Kaiser, B.; Jaegermann, W.; Jafari, A.; Sergueev, I.; Krewald, V.; et al. Substituent Effects in Iron Porphyrin Catalysts for the Hydrogen Evolution Reaction. *Chem. Eur. J.* **2023**, *29*, e202202465. [[CrossRef](#)] [[PubMed](#)]
27. Gawande, M.B.; Ariga, K.; Yamauchi, Y. Single-Atom Catalysts. *Small* **2021**, *17*, 2101584. [[CrossRef](#)] [[PubMed](#)]
28. Agwa, A.M.; El-Fergany, A.A.; Sarhan, G.M. Steady-State Modeling of Fuel Cells Based on Atom Search Optimizer. *Energies* **2019**, *12*, 1884. [[CrossRef](#)]
29. Ding, J.; Yang, H.; Zhang, S.; Liu, Q.; Cao, H.; Luo, J.; Liu, X. Advances in the Electrocatalytic Hydrogen Evolution Reaction by Metal Nanoclusters-based Materials. *Small* **2022**, *18*, 2204524. [[CrossRef](#)] [[PubMed](#)]
30. Chen, S.; Cui, M.; Yin, Z.; Xiong, J.; Mi, L.; Li, Y. Single-Atom and Dual-Atom Electrocatalysts Derived from Metal Organic Frameworks: Current Progress and Perspectives. *ChemSusChem* **2021**, *14*, 73–93. [[CrossRef](#)] [[PubMed](#)]
31. Han, L.; Ou, P.; Liu, W.; Wang, X.; Wang, H.-T.; Zhang, R.; Pao, C.-W.; Liu, X.; Pong, W.-F.; Song, J.; et al. Design of Ru-Ni diatomic sites for efficient alkaline hydrogen oxidation. *Sci. Adv.* **2022**, *8*, eabm3779. [[CrossRef](#)]
32. Cao, H.; Wei, T.; Liu, Q.; Zhang, S.; Qin, Y.; Wang, H.; Luo, J.; Liu, X. Hollow Carbon Cages Derived from Polyoxometalate-Encapsulated Metal-Organic Frameworks for Energy-Saving Hydrogen Production. *ChemCatChem* **2023**. [[CrossRef](#)]
33. Grishakov, K.S.; Katin, K.P.; Kochaev, A.I.; Kaya, S.; Gimaldinova, M.A.; Maslov, M.M. Ab initio Study of Hydrogen Adsorption on Metal-Decorated Borophene-Graphene Bilayer. *Energies* **2021**, *14*, 2473. [[CrossRef](#)]
34. Chen, Y.; Lin, J.; Jia, B.; Wang, X.; Jiang, S.; Ma, T. Isolating Single and Few Atoms for Enhanced Catalysis. *Adv. Mater.* **2022**, *34*, e2201796. [[CrossRef](#)]

35. Jin, M.; Liu, S.; Meng, G.; Zhang, S.; Liu, Q.; Luo, J.; Liu, X. Low-Coordinated Mo Clusters for High-Efficiency Electrocatalytic Hydrogen Peroxide Production. *Adv. Mater. Interfaces* **2023**, *10*, 2201144. [[CrossRef](#)]
36. Hou, X.; Ding, J.; Liu, W.; Zhang, S.; Luo, J.; Liu, X. Asymmetric Coordination Environment Engineering of Atomic Catalysts for CO<sub>2</sub> Reduction. *Nanomaterials* **2023**, *13*, 309. [[CrossRef](#)]
37. Dobrota, A.S.; Skorodumova, N.V.; Mentus, S.V.; Pašti, I.A. Surface pourbaix plots of M@N<sub>4</sub>-graphene single-atom electrocatalysts from density functional theory thermodynamic modeling. *Electrochim. Acta* **2022**, *412*, 140155. [[CrossRef](#)]
38. Chen, S.; Li, X.; Kao, C.-W.; Luo, T.; Chen, K.; Fu, J.; Ma, C.; Li, H.; Li, M.; Chan, T.-S.; et al. Unveiling the Proton-Feeding Effect in Sulfur-Doped Fe-N-C Single-Atom Catalyst for Enhanced CO<sub>2</sub> Electroreduction. *Angew. Chem. Int. Ed.* **2022**, *61*, e202206233.
39. Antil, B.; Kumar, L.; Ranjan, R.; Shenoy, S.; Tarafder, K.; Gopinath, C.S.; Deka, S. One-Dimensional Multichannel g-C<sub>3</sub>N<sub>4.7</sub> Nanostructure Realizing an Efficient Photocatalytic Hydrogen Evolution Reaction and Its Theoretical Investigations. *ACS Appl. Energy Mater.* **2021**, *4*, 3118–3129. [[CrossRef](#)]
40. Cui, J.; Liu, X.; Wei, Y.; Shen, X. A Synergistic effect on the atomic cluster M<sub>4</sub> supported on MN<sub>4</sub>-graphene (M = Fe, Ni) for the hydrogen evolution reaction. *Phys. Chem. Chem. Phys.* **2022**, *24*, 11704–11712. [[CrossRef](#)] [[PubMed](#)]
41. Wei, T.; Liu, W.; Zhang, S.; Liu, Q.; Luo, J.; Liu, X. A dual-functional Bi-doped Co<sub>3</sub>O<sub>4</sub> nanosheet array towards high efficiency 5-hydroxymethylfurfural oxidation and hydrogen production. *Chem. Commun.* **2023**, *59*, 442–445. [[CrossRef](#)]
42. Wang, Y.; Wang, Q.; Wu, J.; Zhao, X.; Xiong, Y.; Luo, F.; Lei, Y. Asymmetric atomic sites make different: Recent progress in electrocatalytic CO<sub>2</sub> reduction. *Nano Energy* **2022**, *103*, 107815. [[CrossRef](#)]
43. Xu, W.; Tang, H.; Gu, H.; Xi, H.; Wu, P.; Liang, B.; Liu, Q.; Chen, W. Research progress of asymmetrically coordinated single-atom catalysts for electrocatalytic reactions. *J. Mater. Chem. A* **2022**, *10*, 14732–14746. [[CrossRef](#)]
44. Yang, M.; Liu, Y.; Sun, J.; Zhang, S.; Liu, X.; Luo, J. Integration of partially phosphatized bimetal centers into trifunctional catalyst for high-performance hydrogen production and flexible Zn-air battery. *Sci. China Mater.* **2022**, *65*, 1176–1186. [[CrossRef](#)]
45. Liu, H.; Fu, J.; Li, H.; Sun, J.; Liu, X.; Qiu, Y.; Peng, X.; Liu, Y.; Bao, H.; Zhuo, L.; et al. Single palladium site in ordered porous heteroatom-doped carbon for high-performance alkaline hydrogen oxidation. *Appl. Catal. B Environ.* **2022**, *306*, 121029. [[CrossRef](#)]
46. Cometto, C.; Ugolotti, A.; Graziotti, E.; Moretto, A.; Bottaro, G.; Armelao, L.; Di Valentin, C.; Calvillo, L.; Granozzi, G. Copper single-atoms embedded in 2D graphitic carbon nitride for the CO<sub>2</sub> reduction. *npj 2D Mater. Appl.* **2021**, *5*, 63. [[CrossRef](#)]
47. Muhyuddin, M.; Zocche, N.; Lorenzi, R.; Ferrara, C.; Poli, F.; Soavi, F.; Santoro, C. Valorization of the inedible pistachio shells into nanoscale transition metal and nitrogen codoped carbon-based electrocatalysts for hydrogen evolution reaction and oxygen reduction reaction. *Mater. Renew. Sustain. Energy* **2022**, *11*, 131–141. [[CrossRef](#)]
48. Li, J.; Hu, J.; Zhang, M.; Gou, W.; Zhang, S.; Chen, Z.; Qu, Y.; Ma, Y. A fundamental viewpoint on the hydrogen spillover phenomenon of electrocatalytic hydrogen evolution. *Nat. Commun.* **2021**, *12*, 3502. [[CrossRef](#)]
49. Ge, S.; Zhang, L.; Hou, J.; Liu, S.; Qin, Y.; Liu, Q.; Cai, X.; Sun, Z.; Yang, M.; Luo, J.; et al. Cu<sub>2</sub>O-Derived PtCu Nanoalloy toward Energy-Efficient Hydrogen Production via Hydrazine Electrolysis under Large Current Density. *ACS Appl. Energy Mater.* **2022**, *5*, 9487–9494. [[CrossRef](#)]
50. Nguyen, T.P.; Kim, I.T. Single-Atom Transition Metal Photocatalysts for Hydrogen Evolution Reactions. *Catalysts* **2022**, *12*, 1304. [[CrossRef](#)]
51. Liu, Z.; Sun, L.; Zhang, Q.; Teng, Z.; Sun, H.; Su, C. TiO<sub>2</sub>-supported Single-atom Catalysts: Synthesis, Structure, and Application. *Chem. Res. Chin. Univ.* **2022**, *38*, 1123–1138. [[CrossRef](#)]
52. Hruby, V.; Zaoralova, D.; Medved, M.; Bakandritsos, A.; Zboril, R.; Otyepka, M. Emerging graphene derivatives as active 2D coordination platforms for single-atom catalysts. *Nanoscale* **2022**, *14*, 13490–13499. [[CrossRef](#)]
53. Zhu, Q.; Xu, Z.; Qiu, B.; Xing, M.; Zhang, J. Emerging Cocatalysts on g-C<sub>3</sub>N<sub>4</sub> for Photocatalytic Hydrogen Evolution. *Small* **2021**, *17*, 2101070. [[CrossRef](#)]
54. Wang, Z.-L.; Hao, X.-F.; Jiang, Z.; Sun, X.-P.; Xu, D.; Wang, J.; Zhong, H.-X.; Meng, F.-L.; Zhang, X.-B. C and N Hybrid Coordination Derived Co-C-N Complex as a Highly Efficient Electrocatalyst for Hydrogen Evolution Reaction. *J. Am. Chem. Soc.* **2015**, *137*, 15070–15073. [[CrossRef](#)] [[PubMed](#)]
55. Di Liberto, G.; Cipriano, L.A.; Pacchioni, G. Role of Dihydride and Dihydrogen Complexes in Hydrogen Evolution Reaction on Single-Atom Catalysts. *J. Am. Chem. Soc.* **2021**, *143*, 20431–20441. [[CrossRef](#)] [[PubMed](#)]
56. Zhang, X.; Li, Y.-A.; Huang, Y.; Mu, H.; Gu, X.; Li, F.; Wang, Z.; Li, J. Impacts of Metal-Support Interaction on Hydrogen Evolution Reaction of Cobalt-Nitride-Carbide Catalyst. *Front. Chem.* **2022**, *9*, 828964. [[CrossRef](#)]
57. Cepitis, R.; Kongi, N.; Grozovski, V.; Ivaništšev, V.; Lust, E. Multifunctional Electrocatalysis on Single-Site Metal Catalysts: A Computational Perspective. *Catalysts* **2021**, *11*, 1165. [[CrossRef](#)]
58. Zang, W.; Sun, T.; Yang, T.; Xi, S.; Waqar, M.; Kou, Z.; Lyu, Z.; Feng, Y.P.; Wang, J.; Pennycook, S.J. Efficient Hydrogen Evolution of Oxidized Ni-N<sub>3</sub> Defective Sites for Alkaline Freshwater and Seawater Electrolysis. *Adv. Mater.* **2021**, *33*, 2003846. [[CrossRef](#)] [[PubMed](#)]
59. Liu, X.; Zheng, L.; Han, C.; Zong, H.; Yang, G.; Lin, S.; Kumar, A.; Jadhav, A.R.; Tran, N.Q.; Hwang, Y.; et al. Identifying the Activity Origin of a Cobalt Single-Atom Catalyst for Hydrogen Evolution Using Supervised Learning. *Adv. Funct. Mater.* **2021**, *31*, 2100547. [[CrossRef](#)]
60. Zhang, L.; Jia, Y.; Gao, G.; Yan, X.; Chen, N.; Chen, J.; Soo, M.T.; Wood, B.; Yang, D.; Du, A.; et al. Graphene Defects Trap Atomic Ni Species for Hydrogen and Oxygen Evolution Reactions. *Chem* **2018**, *4*, 285–297. [[CrossRef](#)]

61. Qiu, H.-J.; Ito, Y.; Cong, W.; Tan, Y.; Liu, P.; Hirata, A.; Fujita, T.; Tang, Z.; Chen, M. Nanoporous Graphene with Single-Atom Nickel Dopants: An Efficient and Stable Catalyst for Electrochemical Hydrogen Production. *Angew. Chem. Int. Ed.* **2015**, *54*, 14031–14035. [[CrossRef](#)] [[PubMed](#)]
62. Fang, S.; Zhu, X.; Liu, X.; Gu, J.; Liu, W.; Wang, D.; Zhang, W.; Lin, Y.; Lu, J.; Wei, S.; et al. Uncovering near-free platinum single-atom dynamics during electrochemical hydrogen evolution reaction. *Nat. Commun.* **2020**, *11*, 1029. [[CrossRef](#)] [[PubMed](#)]
63. Wei, H.; Huang, K.; Wang, D.; Zhang, R.; Ge, B.; Ma, J.; Wen, B.; Zhang, S.; Li, Q.; Lei, M.; et al. Iced photochemical reduction to synthesize atomically dispersed metals by suppressing nanocrystal growth. *Nat. Commun.* **2017**, *8*, 1490. [[CrossRef](#)] [[PubMed](#)]
64. Peng, Y.; Lu, B.; Chen, L.; Wang, N.; Lu, J.E.; Ping, Y.; Chen, S. Hydrogen evolution reaction catalyzed by ruthenium ion-complexed graphitic carbon nitride nanosheets. *J. Mater. Chem. A* **2017**, *5*, 18261–18269. [[CrossRef](#)]
65. Yin, X.-P.; Wang, H.-J.; Tang, S.-F.; Lu, X.-L.; Shu, M.; Si, R.; Lu, T.-B. Engineering the Coordination Environment of Single-Atom Platinum Anchored on Graphdiyne for Optimizing Electrocatalytic Hydrogen Evolution. *Angew. Chem. Int. Ed.* **2018**, *57*, 9382–9386. [[CrossRef](#)] [[PubMed](#)]
66. Lu, B.; Guo, L.; Wu, F.; Peng, Y.; Lu, J.E.; Smart, T.J.; Wang, N.; Finckel, Y.Z.; Morris, D.; Zhang, P.; et al. Ruthenium atomically dispersed in carbon outperforms platinum toward hydrogen evolution in alkaline media. *Nat. Commun.* **2019**, *10*, 631. [[CrossRef](#)]
67. Chen, W.; Pei, J.; He, C.-T.; Wan, J.; Ren, H.; Wang, Y.; Dong, J.; Wu, K.; Cheong, W.-C.; Mao, J.; et al. Single Tungsten Atoms Supported on MOF-Derived N-Doped Carbon for Robust Electrochemical Hydrogen Evolution. *Adv. Mater.* **2018**, *30*, 1800396. [[CrossRef](#)]
68. Lai, W.-H.; Zhang, L.-F.; Hua, W.-B.; Indris, S.; Yan, Z.-C.; Hu, Z.; Zhang, B.; Liu, Y.; Wang, L.; Liu, M.; et al. General  $\pi$ -Electron-Assisted Strategy for Ir, Pt, Ru, Pd, Fe, Ni Single-Atom Electrocatalysts with Bifunctional Active Sites for Highly Efficient Water Splitting. *Angew. Chem. Int. Ed.* **2019**, *58*, 11868–11873. [[CrossRef](#)]
69. Jin, H.; Sultan, S.; Ha, M.; Tiwari, J.N.; Kim, M.G.; Kim, K.S. Simple and Scalable Mechanochemical Synthesis of Noble Metal Catalysts with Single Atoms toward Highly Efficient Hydrogen Evolution. *Adv. Funct. Mater.* **2020**, *30*, 2000531. [[CrossRef](#)]
70. Chen, W.; Pei, J.; He, C.-T.; Wan, J.; Ren, H.; Zhu, Y.; Wang, Y.; Dong, J.; Tian, S.; Cheong, W.-C.; et al. Rational Design of Single Molybdenum Atoms Anchored on N-Doped Carbon for Effective Hydrogen Evolution Reaction. *Angew. Chem. Int. Ed.* **2017**, *56*, 16086–16090. [[CrossRef](#)] [[PubMed](#)]
71. Wan, J.; Zhao, Z.; Shang, H.; Peng, B.; Chen, W.; Pei, J.; Zheng, L.; Dong, J.; Cao, R.; Sarangi, R.; et al. In Situ Phosphatizing of Triphenylphosphine Encapsulated within Metal-Organic Frameworks to Design Atomic Co<sub>1</sub>-P<sub>1</sub>N<sub>3</sub> Interfacial Structure for Promoting Catalytic Performance. *J. Am. Chem. Soc.* **2020**, *142*, 8431–8439. [[CrossRef](#)] [[PubMed](#)]
72. Liu, J.; Wang, D.; Huang, K.; Dong, J.; Liao, J.; Dai, S.; Tang, X.; Yan, M.; Gong, H.; Liu, J.; et al. Iodine-Doping-Induced Electronic Structure Tuning of Atomic Cobalt for Enhanced Hydrogen Evolution Electrocatalysis. *ACS Nano* **2021**, *15*, 18125–18134. [[CrossRef](#)]
73. Li, T.; Lu, T.; Li, X.; Xu, L.; Zhang, Y.; Tian, Z.; Yang, J.; Pang, H.; Tang, Y.; Xue, J. Atomically Dispersed Mo Sites Anchored on Multichannel Carbon Nanofibers toward Superior Electrocatalytic Hydrogen Evolution. *ACS Nano* **2021**, *15*, 20032–20041. [[CrossRef](#)]
74. Gao, X.; Zhou, Y.; Cheng, Z.; Tan, Y.; Liu, S.; Shen, Z. Doping sp-hybridized B atoms in graphyne supported single cobalt atoms for hydrogen evolution electrocatalysis. *Int. J. Hydrogen Energy* **2019**, *44*, 27421–27428. [[CrossRef](#)]
75. Zhou, Y.; Song, E.; Chen, W.; Segre, C.U.; Zhou, J.; Lin, Y.-C.; Zhu, C.; Ma, R.; Liu, P.; Chu, S.; et al. Dual-Metal Interbonding as the Chemical Facilitator for Single-Atom Dispersions. *Adv. Mater.* **2020**, *32*, 2003484. [[CrossRef](#)]
76. Zhang, L.; Si, R.; Liu, H.; Chen, N.; Wang, Q.; Adair, K.; Wang, Z.; Chen, J.; Song, Z.; Li, J.; et al. Atomic layer deposited Pt-Ru dual-metal dimers and identifying their active sites for hydrogen evolution reaction. *Nat. Commun.* **2019**, *10*, 4936. [[CrossRef](#)]
77. Hu, C.; Song, E.; Wang, M.; Chen, W.; Huang, F.; Feng, Z.; Liu, J.; Wang, J. Partial-Single-Atom, Partial-Nanoparticle Composites Enhance Water Dissociation for Hydrogen Evolution. *Adv. Sci.* **2021**, *8*, 2001881. [[CrossRef](#)]
78. Zeng, X.; Shui, J.; Liu, X.; Liu, Q.; Li, Y.; Shang, J.; Zheng, L.; Yu, R. Single-Atom to Single-Atom Grafting of Pt<sub>1</sub> onto Fe-N<sub>4</sub> Center: Pt<sub>1</sub>@Fe-N-C Multifunctional Electrocatalyst with Significantly Enhanced Properties. *Adv. Energy Mater.* **2018**, *8*, 1701345. [[CrossRef](#)]
79. Yang, Y.; Qian, Y.; Li, H.; Zhang, Z.; Mu, Y.; Do, D.; Zhou, B.; Dong, J.; Yan, W.; Qin, Y.; et al. O-coordinated W-Mo dual-atom catalyst for pH-universal electrocatalytic hydrogen evolution. *Sci. Adv.* **2020**, *6*, eaba6586. [[CrossRef](#)] [[PubMed](#)]
80. Huang, H.; Zhao, Y.; Bai, Y.; Li, F.; Zhang, Y.; Chen, Y. Conductive Metal-Organic Frameworks with Extra Metallic Sites as an Efficient Electrocatalyst for the Hydrogen Evolution Reaction. *Adv. Sci.* **2020**, *7*, 2000012. [[CrossRef](#)]
81. Wu, Y.-P.; Zhou, W.; Zhao, J.; Dong, W.-W.; Lan, Y.-Q.; Li, D.-S.; Sun, C.; Bu, X. Surfactant-Assisted Phase-Selective Synthesis of New Cobalt MOFs and Their Efficient Electrocatalytic Hydrogen Evolution Reaction. *Angew. Chem. Int. Ed.* **2017**, *56*, 13001–13005. [[CrossRef](#)]
82. Lin, H.-W.; Senthil Raja, D.; Chuah, X.-F.; Hsieh, C.-T.; Chen, Y.-A.; Lu, S.-Y. Bi-metallic MOFs possessing hierarchical synergistic effects as high performance electrocatalysts for overall water splitting at high current densities. *Appl. Catal. B Environ.* **2019**, *258*, 118023. [[CrossRef](#)]
83. Zhang, L.; Li, S.; Gómez-García, C.J.; Ma, H.; Zhang, C.; Pang, H.; Li, B. Two Novel Polyoxometalate-Encapsulated Metal-Organic Nanotube Frameworks as Stable and Highly Efficient Electrocatalysts for Hydrogen Evolution Reaction. *ACS Appl. Mater. Interfaces* **2018**, *10*, 31498–31504. [[CrossRef](#)]

84. Chao, T.; Luo, X.; Chen, W.; Jiang, B.; Ge, J.; Lin, Y.; Wu, G.; Wang, X.; Hu, Y.; Zhuang, Z.; et al. Atomically Dispersed Copper-Platinum Dual Sites Alloyed with Palladium Nanorings Catalyze the Hydrogen Evolution Reaction. *Angew. Chem. Int. Ed.* **2017**, *56*, 16047–16051. [[CrossRef](#)] [[PubMed](#)]
85. Cao, L.; Luo, Q.; Liu, W.; Lin, Y.; Liu, X.; Cao, Y.; Zhang, W.; Wu, Y.; Yang, J.; Yao, T.; et al. Identification of single-atom active sites in carbon-based cobalt catalysts during electrocatalytic hydrogen evolution. *Nat. Catal.* **2019**, *2*, 134–141. [[CrossRef](#)]
86. Liang, H.-W.; Brüller, S.; Dong, R.; Zhang, J.; Feng, X.; Müllen, K. Molecular metal-N<sub>x</sub> centres in porous carbon for electrocatalytic hydrogen evolution. *Nat. Commun.* **2015**, *6*, 7992. [[CrossRef](#)] [[PubMed](#)]
87. Fei, H.; Dong, J.; Wan, C.; Zhao, Z.; Xu, X.; Lin, Z.; Wang, Y.; Liu, H.; Zang, K.; Luo, J.; et al. Microwave-Assisted Rapid Synthesis of Graphene-Supported Single Atomic Metals. *Adv. Mater.* **2018**, *30*, 1802146. [[CrossRef](#)]
88. Zhang, H.; An, P.; Zhou, W.; Guan, B.Y.; Zhang, P.; Dong, J.; Lou, X.W. Dynamic traction of lattice-confined platinum atoms into mesoporous carbon matrix for hydrogen evolution reaction. *Sci. Adv.* **2018**, *4*, eaa06657. [[CrossRef](#)]
89. Ye, S.; Luo, F.; Zhang, Q.; Zhang, P.; Xu, T.; Wang, Q.; He, D.; Guo, L.; Zhang, Y.; He, C.; et al. Highly stable single Pt atomic sites anchored on aniline-stacked graphene for hydrogen evolution reaction. *Energy Environ. Sci.* **2019**, *12*, 1000–1007. [[CrossRef](#)]
90. Li, T.; Liu, J.; Song, Y.; Wang, F. Photochemical Solid-Phase Synthesis of Platinum Single Atoms on Nitrogen-Doped Carbon with High Loading as Bifunctional Catalysts for Hydrogen Evolution and Oxygen Reduction Reactions. *ACS Catal.* **2018**, *8*, 8450–8458. [[CrossRef](#)]
91. Liu, D.; Li, X.; Chen, S.; Yan, H.; Wang, C.; Wu, C.; Haleem, Y.A.; Duan, S.; Lu, J.; Ge, B.; et al. Atomically dispersed platinum supported on curved carbon supports for efficient electrocatalytic hydrogen evolution. *Nat. Energy* **2019**, *4*, 512–518. [[CrossRef](#)]
92. Wang, S.; Wang, M.; Liu, Z.; Liu, S.; Chen, Y.; Li, M.; Zhang, H.; Wu, Q.; Guo, J.; Feng, X.; et al. Synergetic Function of the Single-Atom Ru-N<sub>4</sub> Site and Ru Nanoparticles for Hydrogen Production in a Wide pH Range and Seawater Electrolysis. *ACS Appl. Mater. Interfaces* **2022**, *14*, 15250–15258. [[CrossRef](#)]
93. Yang, J.; Chen, B.; Liu, X.; Liu, W.; Li, Z.; Dong, J.; Chen, W.; Yan, W.; Yao, T.; Duan, X.; et al. Efficient and Robust Hydrogen Evolution: Phosphorus Nitride Imide Nanotubes as Supports for Anchoring Single Ruthenium Sites. *Angew. Chem. Int. Ed.* **2018**, *57*, 9495–9500. [[CrossRef](#)] [[PubMed](#)]
94. Lei, C.; Wang, Y.; Hou, Y.; Liu, P.; Yang, J.; Zhang, T.; Zhuang, X.; Chen, M.; Yang, B.; Lei, L.; et al. Efficient alkaline hydrogen evolution on atomically dispersed Ni-N<sub>x</sub> species anchored porous carbon with embedded Ni nanoparticles by accelerating water dissociation kinetics. *Energy Environ. Sci.* **2019**, *12*, 149–156. [[CrossRef](#)]
95. Hou, J.; Peng, X.; Sun, J.; Zhang, S.; Liu, Q.; Wang, X.; Luo, J.; Liu, X. Accelerating hydrazine-assisted hydrogen production kinetics with Mn dopant modulated Co<sub>2</sub> nanowire arrays. *Inorg. Chem. Front.* **2022**, *9*, 3047–3058. [[CrossRef](#)]
96. Hu, G.; Wu, Z.; Jiang, D.-e. Stronger-than-Pt hydrogen adsorption in a Au<sub>22</sub> nanocluster for the hydrogen evolution reaction. *J. Mater. Chem. A* **2018**, *6*, 7532–7537. [[CrossRef](#)]
97. Hossain, M.D.; Liu, Z.; Zhuang, M.; Yan, X.; Xu, G.-L.; Gadre, C.A.; Tyagi, A.; Abidi, I.H.; Sun, C.-J.; Wong, H.; et al. Rational Design of Graphene-Supported Single Atom Catalysts for Hydrogen Evolution Reaction. *Adv. Energy Mater.* **2019**, *9*, 1803689. [[CrossRef](#)]
98. Shen, H.; Wei, T.; Liu, Q.; Zhang, S.; Luo, J.; Liu, X. Heterogeneous Ni-MoN nanosheet-assembled microspheres for urea-assisted hydrogen production. *J. Colloid Interface Sci.* **2023**, *634*, 730–736. [[CrossRef](#)]
99. Cui, X.; Gao, L.; Lu, C.-H.; Ma, R.; Yang, Y.; Lin, Z. Rational coordination regulation in carbon-based single-metal-atom catalysts for electrocatalytic oxygen reduction reaction. *Nano Convergence* **2022**, *9*, 34. [[CrossRef](#)] [[PubMed](#)]
100. Ida, S.; Sato, K.; Nagata, T.; Hagiwara, H.; Watanabe, M.; Kim, N.; Shiota, Y.; Koinuma, M.; Takenaka, S.; Sakai, T.; et al. A Cocatalyst that Stabilizes a Hydride Intermediate during Photocatalytic Hydrogen Evolution over a Rhodium-Doped TiO<sub>2</sub> Nanosheet. *Angew. Chem. Int. Ed.* **2018**, *57*, 9073–9077. [[CrossRef](#)]
101. Gao, S.; Wei, T.; Sun, J.; Liu, Q.; Ma, D.; Liu, W.; Zhang, S.; Luo, J.; Liu, X. Atomically Dispersed Metal-Based Catalysts for Zn-CO<sub>2</sub> Batteries. *Small Struct.* **2022**, *3*, 2200086. [[CrossRef](#)]
102. Fu, W.; Wang, Y.; Tian, W.; Zhang, H.; Li, J.; Wang, S.; Wang, Y. Non-Metal Single-Phosphorus-Atom Catalysis of Hydrogen Evolution. *Angew. Chem. Int. Ed.* **2020**, *59*, 23791–23799. [[CrossRef](#)] [[PubMed](#)]
103. Quan, Z.; Kang, L.; Gaocan, Q.; Shusheng, Z.; Qian, L.; Yang, L.; Jun, L.; Xijun, L. High Entropy Alloys in Water Electrolysis: Recent advances, Fundamentals, and Challenges. *Sci. China Mater.* **2022**. [[CrossRef](#)]
104. Huan, T.N.; Ranjbar, N.; Rousse, G.; Sougrati, M.; Zitolo, A.; Mougél, V.; Jaouen, F.; Fontecave, M. Electrochemical Reduction of CO<sub>2</sub> Catalyzed by Fe-N-C Materials: A Structure–Selectivity Study. *ACS Catal.* **2017**, *7*, 1520–1525. [[CrossRef](#)]
105. Gao, S.; Wang, T.; Jin, M.; Zhang, S.; Liu, Q.; Hu, G.; Yang, H.; Luo, J.; Liu, X. Bifunctional Nb-N-C atomic catalyst for aqueous Zn-air battery driving CO<sub>2</sub> electrolysis. *Sci. China Mater.* **2022**. [[CrossRef](#)]
106. Maher, A.G.; Passard, G.; Dogutan, D.K.; Halbach, R.L.; Anderson, B.L.; Gagliardi, C.J.; Taniguchi, M.; Lindsey, J.S.; Nocera, D.G. Hydrogen Evolution Catalysis by a Sparsely Substituted Cobalt Chlorin. *ACS Catal.* **2017**, *7*, 3597–3606. [[CrossRef](#)]
107. Meng, G.; Cao, H.; Wei, T.; Liu, Q.; Fu, J.; Zhang, S.; Luo, J.; Liu, X. Highly dispersed Ru clusters toward an efficient and durable hydrogen oxidation reaction. *Chem. Commun.* **2022**, *58*, 11839–11842. [[CrossRef](#)]
108. Hu, B.; Huang, A.; Zhang, X.; Chen, Z.; Tu, R.; Zhu, W.; Zhuang, Z.; Chen, C.; Peng, Q.; Li, Y. Atomic Co/Ni dual sites with N/P-coordination as bifunctional oxygen electrocatalyst for rechargeable zinc-air batteries. *Nano Res.* **2021**, *14*, 3482–3488. [[CrossRef](#)]

109. Zhu, P.; Xiong, X.; Wang, D. Regulations of active moiety in single atom catalysts for electrochemical hydrogen evolution reaction. *Nano Res.* **2022**, *15*, 5792–5815. [[CrossRef](#)]
110. Ge, M.; Mengmeng, J.; Tianran, W.; Qian, L.; Shusheng, Z.; Xianyun, P.; Jun, L.; Xijun, L. MoC nanocrystals confined in N-doped carbon nanosheets toward highly selective electrocatalytic nitric oxide reduction to ammonia. *Nano Res.* **2022**, *15*, 8890–8896. [[CrossRef](#)]
111. Sahoo, S.K.; Ye, Y.; Lee, S.; Park, J.; Lee, H.; Lee, J.; Han, J.W. Rational Design of TiC-Supported Single-Atom Electrocatalysts for Hydrogen Evolution and Selective Oxygen Reduction Reactions. *ACS Energy Lett.* **2019**, *4*, 126–132. [[CrossRef](#)]
112. Meng, G.; Wei, T.; Liu, W.; Li, W.; Zhang, S.; Liu, W.; Liu, Q.; Bao, H.; Luo, J.; Liu, X. NiFe layered double hydroxide nanosheet array for high-efficiency electrocatalytic reduction of nitric oxide to ammonia. *Chem. Commun.* **2022**, *58*, 8097–8100. [[CrossRef](#)]
113. Cao, X.; Zhao, L.; Wulan, B.; Tan, D.; Chen, Q.; Ma, J.; Zhang, J. Atomic Bridging Structure of Nickel–Nitrogen–Carbon for Highly Efficient Electrocatalytic Reduction of CO<sub>2</sub>. *Angew. Chem. Int. Ed.* **2022**, *61*, e202113918.
114. Kwon, I.S.; Kwak, I.H.; Debela, T.T.; Abbas, H.G.; Park, Y.C.; Ahn, J.-p.; Park, J.; Kang, H.S. Se-Rich MoSe<sub>2</sub> Nanosheets and Their Superior Electrocatalytic Performance for Hydrogen Evolution Reaction. *ACS Nano* **2020**, *14*, 6295–6304. [[CrossRef](#)] [[PubMed](#)]
115. Chen, D.; Zhang, L.-H.; Du, J.; Wang, H.; Guo, J.; Zhan, J.; Li, F.; Yu, F. A Tandem Strategy for Enhancing Electrochemical CO<sub>2</sub> Reduction Activity of Single-Atom Cu-S<sub>1</sub>N<sub>3</sub> Catalysts via Integration with Cu Nanoclusters. *Angew. Chem. Int. Ed.* **2021**, *60*, 24022–24027. [[CrossRef](#)] [[PubMed](#)]
116. Zhou, Z.-H.; Li, W.-H.; Zhang, Z.; Zhao, X.-C.; Cao, W.; Huang, Q.-S. Ni optimizes Ir reaction pathway through IrNi alloy synergistic effect to improve overall water splitting efficiency. *Int. J. Hydrogen Energy* **2023**, *48*, 8440–8449. [[CrossRef](#)]
117. Yang, M.; Liu, S.; Sun, J.; Jin, M.; Fu, R.; Zhang, S.; Li, H.; Sun, Z.; Luo, J.; Liu, X. Highly dispersed Bi clusters for efficient rechargeable Zn–CO<sub>2</sub> batteries. *Appl. Catal. B: Environ.* **2022**, *307*, 121145. [[CrossRef](#)]
118. Wang, H.; Zhang, F.; Jin, M.; Zhao, D.; Fan, X.; Li, Z.; Luo, Y.; Zheng, D.; Li, T.; Wang, Y.; et al. V-doped TiO<sub>2</sub> nanobelt array for high-efficiency electrocatalytic nitrite reduction to ammonia. *Mater. Today Phys.* **2023**, *30*, 100944. [[CrossRef](#)]
119. Fu, W.; Wang, Y.; Hu, J.; Zhang, H.; Luo, P.; Sun, F.; Ma, X.; Huang, Z.; Li, J.; Guo, Z.; et al. Surface-Electron Coupling for Efficient Hydrogen Evolution. *Angew. Chem. Int. Ed.* **2019**, *58*, 17709–17717. [[CrossRef](#)]
120. Tkachenko, P.; Volchek, V.; Kurenkova, A.; Gerasimov, E.; Popovetskiy, P.; Asanov, I.; Yushina, I.; Kozlova, E.; Vasilchenko, D. Photocatalytic H<sub>2</sub> generation from ethanol and glucose aqueous solutions by PtO<sub>x</sub>/TiO<sub>2</sub> composites. *Int. J. Hydrogen Energy* **2022**. [[CrossRef](#)]
121. Wang, T.; Gao, S.; Wei, T.; Qin, Y.; Zhang, S.; Ding, J.; Liu, Q.; Luo, J.; Liu, X. Co nanoparticles confined in mesoporous Mo/N co-doped polyhedral carbon frameworks towards high-efficiency oxygen reduction. *Chem. Eur. J.* **2023**. [[CrossRef](#)] [[PubMed](#)]
122. Zhang, L.-N.; Li, R.; Zang, H.-Y.; Tan, H.-Q.; Kang, Z.-H.; Wang, Y.-H.; Li, Y.-G. Advanced hydrogen evolution electrocatalysts promising sustainable hydrogen and chlor-alkali co-production. *Energy Environ. Sci.* **2021**, *14*, 6191–6210. [[CrossRef](#)]
123. Kwak, I.H.; Abbas, H.G.; Kwon, I.S.; Park, Y.C.; Seo, J.; Cho, M.K.; Ahn, J.-P.; Seo, H.W.; Park, J.; Kang, H.S. Intercalation of cobaltocene into WS<sub>2</sub> nanosheets for enhanced catalytic hydrogen evolution reaction. *J. Mater. Chem. A* **2019**, *7*, 8101–8106. [[CrossRef](#)]
124. Wei, T.; Bao, H.; Wang, X.; Zhang, S.; Liu, Q.; Luo, J.; Liu, X. Ionic Liquid-Assisted Electrocatalytic NO Reduction to NH<sub>3</sub> by P-Doped MoS<sub>2</sub>. *ChemCatChem* **2023**, *15*, e202201411. [[CrossRef](#)]
125. Wang, D.; Jiang, X.; Lin, Z.; Zeng, X.; Zhu, Y.; Wang, Y.; Gong, M.; Tang, Y.; Fu, G. Ethanol-Induced Hydrogen Insertion in Ultrafine IrPdH Boosts pH-Universal Hydrogen Evolution. *Small* **2022**, *18*, 2204063. [[CrossRef](#)]
126. Sultán, S.; Tiwari, J.N.; Singh, A.N.; Zhumagali, S.; Ha, M.; Myung, C.W.; Thangavel, P.; Kim, K.S. Single Atoms and Clusters Based Nanomaterials for Hydrogen Evolution, Oxygen Evolution Reactions, and Full Water Splitting. *Adv. Energy Mater.* **2019**, *9*, 1900624. [[CrossRef](#)]
127. Yang, M.; Sun, J.; Qin, Y.; Yang, H.; Zhang, S.; Liu, X.; Luo, J. Hollow CoFe-layered double hydroxide polyhedrons for highly efficient CO<sub>2</sub> electrolysis. *Sci. China Mater.* **2022**, *65*, 536–542. [[CrossRef](#)]
128. Li, B.; Yu, S.; Zhou, M.; Chen, C.; Lai, C.; Zhang, M.; Lin, H. Graphynes: Ideal supports of single atoms for electrochemical energy conversion. *J. Mater. Chem. A* **2022**, *10*, 3905–3932. [[CrossRef](#)]
129. Wang, X.; Liu, S.; Zhang, H.; Zhang, S.; Meng, G.; Liu, Q.; Sun, Z.; Luo, J.; Liu, X. Polycrystalline SnS<sub>x</sub> nanofilm enables CO<sub>2</sub> electroreduction to formate with high current density. *Chem. Commun.* **2022**, *58*, 7654–7657. [[CrossRef](#)]
130. Tee, S.Y.; Win, K.Y.; Teo, W.S.; Koh, L.-D.; Liu, S.; Teng, C.P.; Han, M.-Y. Recent Progress in Energy-Driven Water Splitting. *Adv. Sci.* **2017**, *4*, 1600337. [[CrossRef](#)] [[PubMed](#)]
131. Li, H.; Zhu, H.; Zhuang, Z.; Lu, S.; Duan, F.; Du, M. Single-atom catalysts for electrochemical clean energy conversion: Recent progress and perspectives. *Sustain. Energy Fuels* **2020**, *4*, 996–1011. [[CrossRef](#)]
132. Liu, S.; Wang, L.; Yang, H.; Gao, S.; Liu, Y.; Zhang, S.; Chen, Y.; Liu, X.; Luo, J. Nitrogen-Doped Carbon Polyhedrons Confined Fe-P Nanocrystals as High-Efficiency Bifunctional Catalysts for Aqueous Zn-CO<sub>2</sub> Batteries. *Small* **2022**, *18*, 2104965. [[CrossRef](#)]
133. Zhu, J.; Cai, L.; Tu, Y.; Zhang, L.; Zhang, W. Emerging ruthenium single-atom catalysts for the electrocatalytic hydrogen evolution reaction. *J. Mater. Chem. A* **2022**, *10*, 15370–15389. [[CrossRef](#)]
134. Steier, L.; Holliday, S. A bright outlook on organic photoelectrochemical cells for water splitting. *J. Mater. Chem. A* **2018**, *6*, 21809–21826. [[CrossRef](#)]
135. Lu, G.; Wang, Z.; Zhang, S.; Ding, J.; Luo, J.; Liu, X. Cathode materials for halide-based aqueous redox flow batteries: Recent progress and future perspectives. *Nanoscale* **2023**, *15*, 4250–4260. [[CrossRef](#)]

136. Zheng, Y.; Chen, S.; Yu, X.; Li, K.; Ni, X.; Ye, L. Nitrogen-doped carbon spheres with precisely-constructed pyridinic-N active sites for efficient oxygen reduction. *Appl. Surf. Sci.* **2022**, *598*, 153786. [[CrossRef](#)]
137. Tiwari, J.N.; Singh, A.N.; Sultan, S.; Kim, K.S. Recent Advancement of p- and d-Block Elements, Single Atoms, and Graphene-Based Photoelectrochemical Electrodes for Water Splitting. *Adv. Energy Mater.* **2020**, *10*, 2000280. [[CrossRef](#)]
138. Hoa, V.H.; Tran, D.T.; Prabhakaran, S.; Kim, D.H.; Hameed, N.; Wang, H.; Kim, N.H.; Lee, J.H. Ruthenium single atoms implanted continuous MoS<sub>2</sub>-Mo<sub>2</sub>C heterostructure for high-performance and stable water splitting. *Nano Energy* **2021**, *88*, 106277. [[CrossRef](#)]
139. Wei, T.; Zhang, S.; Liu, Q.; Qiu, Y.; Luo, J.; Liu, X. Oxygen Vacancy-Rich Amorphous Copper Oxide Enables Highly Selective Electroreduction of Carbon Dioxide to Ethylene. *Acta Phys. Chim. Sin.* **2023**, *39*, 202207026. [[CrossRef](#)]
140. Wang, Z.; Yang, Y.; Zhang, W.; Chen, Y.; Peng, X.; Wang, X.; Zhao, W.; Qin, C.; Liu, Q.; Liu, X.; et al. Single-Atomic Co-B<sub>2</sub>N<sub>2</sub> Sites Anchored on Carbon Nanotube Arrays Promote Lithium Polysulfide Conversion in Lithium Sulfur Batteries. *Carbon Energy* **2022**. [[CrossRef](#)]
141. Liu, W.; Feng, J.; Yin, R.; Ni, Y.; Zheng, D.; Que, W.; Niu, X.; Dai, X.; Shi, W.; Wu, F.; et al. Tailoring oxygenated groups of monolithic cobalt-nitrogen-carbon frameworks for highly efficient hydrogen peroxide production in acidic media. *Chem. Eng. J.* **2022**, *430*, 132990. [[CrossRef](#)]
142. Feng, J.; Zheng, D.; Yin, R.; Niu, X.; Xu, X.; Meng, S.; Ma, S.; Shi, W.; Wu, F.; Liu, W.; et al. A Wide-Temperature Adaptive Aqueous Zinc-Air Battery-Based on Cu-Co Dual Metal-Nitrogen-Carbon/Nanoparticle Electrocatalysts. *Small Struct.* **2023**, *2200340*. [[CrossRef](#)]
143. Zhang, W.; Qin, X.; Wei, T.; Liu, Q.; Luo, J.; Liu, X. Single atomic cerium sites anchored on nitrogen-doped hollow carbon spheres for highly selective electroreduction of nitric oxide to ammonia. *J. Colloid Interface Sci.* **2023**, *638*, 650–657. [[CrossRef](#)]
144. Jin, J.; Chen, F.; Feng, Y.; Zhou, J.; Lei, W.; Gao, F. Co-Ni-Mo phosphides hierarchical nanoarrays as bifunctional electrocatalysts for excellent overall water splitting. *Fuel* **2023**, *332*, 126131. [[CrossRef](#)]
145. Li, W.; Deng, Y.; Luo, L.; Du, Y.; Cheng, X.; Wu, Q. Nitrogen-doped Fe<sub>2</sub>O<sub>3</sub>/NiTe<sub>2</sub> as an excellent bifunctional electrocatalyst for overall water splitting. *J. Colloid Interface Sci.* **2023**, *639*, 416–423. [[CrossRef](#)] [[PubMed](#)]
146. Qin, Y.; Han, X.; Li, Y.; Han, A.; Liu, W.; Xu, H.; Liu, J. Hollow Mesoporous Metal-Organic Frameworks with Enhanced Diffusion for Highly Efficient Catalysis. *ACS Catal.* **2020**, *10*, 5973–5978. [[CrossRef](#)]
147. Lu, M.; Li, L.; Chen, D.; Li, J.; Klyui, N.I.; Han, W. MOF-derived nitrogen-doped CoO@CoP arrays as bifunctional electrocatalysts for efficient overall water splitting. *Electrochim. Acta* **2020**, *330*, 135210. [[CrossRef](#)]
148. Yang, H.; Ma, D.; Li, Y.; Zhao, Q.; Pan, F.; Zheng, S.; Lou, Z. Mo Doped Ru-based Cluster to Promote Alkaline Hydrogen Evolution with Ultra-Low Ru Loading. *Chin. J. Struct. Chem.* **2023**, 100031. [[CrossRef](#)]
149. Wang, X.; Zhang, J.; Wang, Z.; Lin, Z.; Shen, S.; Zhong, W. Fabricating Ru single atoms and clusters on CoP for boosted hydrogen evolution reaction. *Chin. J. Struct. Chem.* **2023**, 100035. [[CrossRef](#)]
150. Liu, W.; Que, W.; Yin, R.; Dai, J.; Zheng, D.; Feng, J.; Xu, X.; Wu, F.; Shi, W.; Liu, X.; et al. Ferrum-molybdenum dual incorporated cobalt oxides as efficient bifunctional anti-corrosion electrocatalyst for seawater splitting. *Appl. Catal. B Environ.* **2023**, *328*, 122488. [[CrossRef](#)]

**Disclaimer/Publisher's Note:** The statements, opinions and data contained in all publications are solely those of the individual author(s) and contributor(s) and not of MDPI and/or the editor(s). MDPI and/or the editor(s) disclaim responsibility for any injury to people or property resulting from any ideas, methods, instructions or products referred to in the content.